

I. PAPAIOANNOU

# Experimental and numerical study on the optimisation of insulated rail joint dynamic behaviour





# **Experimental and numerical study on the optimisation of insulated rail joint dynamic behaviour**

By

Ioannis Papaioannou

in partial fulfilment of the requirements for the degree of

**Master of Science**

in Civil Engineering

at the Delft University of Technology,

to be defended publicly on Wednesday October 3, 2018 at 2:30 PM.

Promoter: Prof. Dr. Ir. Rolf Dollevoet, TU Delft

Thesis committee: Prof. Dr. Ir. Zili Li, TU Delft

Dr. Ir. Zhen Yang, TU Delft

Dr. Ir. Karel van Dalen, TU Delft

Dr. Ir. Edwin Gelinck, ProRail B.V

An electronic version of this thesis is available at <http://repository.tudelft.nl/>.





# Preface

This thesis is the final report of the study “Experimental and numerical study on the optimisation of insulated rail joint dynamic behaviour”, which I carried out for ProRail B.V as M.Sc. – graduation candidate in order to finish my studies at the faculty of Civil Engineering and Geosciences, at Delft University of Technology.

I would like to thank Professor Rolf Dollevoet and Professor Zili Li for their valuable advices and helpful comments which helped me stay enthusiastic and constantly improve my work, but also for giving me the chance to attend the Contact Mechanics Conference 2018. I would like also to thank Professor Dollevoet for the idea that he gave me, to apply as a volunteer, out of which a new friendship was created, but I also improved my Dutch.

I would like also to express my appreciation to my ProRail supervisor Dr. Ir. Edwin Gelinck for his continuous guidance and freedom at the same time, and for trusting me and my ideas even though sometimes he did not get enough feedback from me. I also want to thank him for always including me in all the ProRail meetings and presentations that were beneficial for my career in railway engineering.

A heartfelt thanks to Dr. Ir. Karel Van Dalen for his kindness and his contribution during my thesis and for being a member of my assessment committee.

Of course, despite it being an individual’s research, this could not have happened without the contribution of my daily supervisor Dr. Ir. Zhen Yang. He was always available for me, always willing to answer my questions, and he gave valuable solutions to many of my problems during the thesis. His guidance pushed me to consider aspects of problems that I would not think of at first.

I also want to thank ProRail for making the measurements possible. My sincere appreciation to all my colleagues in ProRail for making me feel like a member of the team from the first day.

Last but not least I would like to thank my family for their continuously unconditional support and for always believing in me. They gave me motivation to keep going every day and taught me never to give up. I would have never come so far with my academic career without their support.

*Ioannis Papaioannou  
Delft, October 2018*



# Table of contents

<b>Preface</b> .....	v
<b>Abstract</b> .....	ix
<b>Nomenclature</b> .....	x
<b>Table of figures</b> .....	xii
<b>1. Introduction</b> .....	1
1.1 General.....	1
1.2 Function of the IRJ.....	1
1.3 Problem statement.....	4
1.4 Research objective.....	7
1.5 Novelty of this research.....	8
1.6 Overall approach.....	8
1.7 Assumptions and limitations.....	8
1.8 Structure of this thesis.....	9
<b>2. Background &amp; Literature review</b> .....	10
2.1 Previous models.....	10
2.2 Vertical track dynamics.....	12
2.2.1 Vibration of the track (40Hz-400Hz).....	12
2.2.2 Vibration of the rail (400Hz-3000Hz).....	13
2.3 Identifying track dynamics using hammer tests.....	14
2.4 Influence of sleeper span on the dynamic behaviour of the track.....	19
2.5 Optimisation of the behaviour of IRJ.....	19
2.6 Fibre-reinforced plastics.....	20
<b>3. Field measurements</b> .....	22
3.1 Location.....	22
3.2 Track site.....	23
3.3 Set-up of the hammer test.....	24
3.4 Measurements procedure – post processing.....	25
3.5 Distance of the sleepers.....	26
3.6 Comparison of the behaviour of the NRG-joint and the normal-joint.....	28
<b>4. Finite element model</b> .....	29
4.1 3D FE model.....	29
4.1.1 Geometry modelling.....	29
4.1.2 Element type – material model.....	30
4.1.3 Constrains.....	31

4.1.4	Load.....	31
4.1.5	Mesh .....	32
4.1.6	Mechanical properties of the track components .....	32
4.1.7	Contact.....	34
4.2	ANSYS – LS DYNA simulation process .....	35
4.3	Calibration of the numerical model/ Deriving track parameters .....	38
4.4	Effect of the system parameters .....	40
4.5	Validation of the transfer accelerances.....	42
4.6	Concluding remarks .....	43
<b>5.</b>	<b>Performance optimisation .....</b>	<b>44</b>
5.1	Pinned-pinned resonance .....	44
5.2	Optimisation of sleepers distribution .....	45
5.3	Concluding remarks .....	47
<b>6.</b>	<b>Conclusions &amp; recommendations .....</b>	<b>48</b>
6.1	Conclusions.....	48
6.2	Recommendations .....	49
<b>Appendices</b>	.....	<b>50</b>
	Appendix A: ANSYS elements .....	50
	SOLID185 Element Description [54].....	50
	SOLID164 Element Description .....	50
	COMBIN14 Element Description [55] .....	51
	COMBI165 Element Description .....	51
	CONTA174 Element Description.....	51
	TARGE170 Element Description .....	52
	Appendix B: Augmented Lagrange Method [56] .....	52
<b>References</b>	.....	<b>54</b>

# Abstract

Sustainable railway systems with less disturbance are highly desired. Insulated rail joint (IRJ) is one important structural component in a railway track. IRJs serve the railway system with two crucial functions: dividing track into sections for signal control and enable the detection of broken rails. An IRJ generally consists of two fishplates, insulation layers between the rails and the fishplates, and an end-post layer between two rails. The fishplates are assembled using pre-tensioned bolts. Although the IRJ plays an important role in the railway system, it introduces discontinuities in stiffness and geometry to wheel-rail rolling contact and is thus considered one of the weakest parts of the railway track. Maintenance of IRJs has been an issue of great concern for the rail operators worldwide. Over the past few years many studies have been conducted on monitoring, modelling and analysis of IRJs. Both numerical and experimental studies have been performed in order to gain better understanding of the behaviour of IRJs under static and dynamic loads. Considering that dynamic wheel-rail impacts occur at IRJs, the dynamic behaviour of IRJs should be carefully examined.

This M.Sc. thesis studies the dynamic behaviour of the IRJ experimentally and numerically. Two three-dimensional finite element (FE) track models with different types of IRJ, i.e. a new NRG-joint and normal joint, are developed. Rails, fishplates, insulation layer and sleepers are represented in the models as detailed as possible, while the rail-pads and the ballast are simplified as spring and damper elements. The NRG-joint consists of two fishplates and six pretensioned bolts, while the normal joint consists of two shorter fishplates and four bolts. Implicit FE analyses are first performed to calculate the initial stresses and displacements of the track models, which are then used as initial conditions for the explicit dynamic FE analysis. Field hammer tests are performed on the track line between Zwolle and Meppel. The tests are used on one hand to calibrate the stiffness and damping parameters involved in the rail-pad and ballast models, and on the other hand to validate the dynamic behaviour reproduced by the FE IRJ models. The comparison between the simulation and the measurements shows reasonable agreement of the results. Based on the validated FE models, optimisation strategies of the dynamic behaviour of the IRJ are proposed by a parametric study. The varied parameters include stiffness and damping of the rail-pads and the ballast as well as sleeper span. Implementation of non-uniform sleeper span seems effective for reducing pinned-pinned resonance. Finally, conclusions are drawn and recommendations for further research are made.

# Nomenclature

## List of acronyms

ANSYS	Analysis System
APDL	ANSYS Parametric Design Language
AutoCAD	Automatic Computer Aided Design
FEM	Finite Element Method
FRF	Frequency Response Function
FRP	Fibre-Reinforced Plastic
IGES	Initial Graphics Exchange Specification
IRJ	Insulated Rail Joint
NDT	Non-Destructive Test
NRG	eNeRGie
PA	Polyamide
PTFE	Polytetrafluoroethylene
UIC	Union Internationale de Chemins de fer (International Union of Railways)

## Greek symbols

$\Delta t$	time step (s)
$\varepsilon$	strain
$\lambda$	wavelength
$\nu_f$	glass fibres Poisson's ratio
$\nu_m$	epoxy Poisson's ratio
$\rho_c$	fiberglass epoxy (composite) density ( $\text{kg/m}^3$ )
$\rho_f$	glass fibres density ( $\text{kg/m}^3$ )
$\rho_m$	epoxy density ( $\text{kg/m}^3$ )
$\Sigma$	summation operator
$\sigma$	stress (MPa)

## Latin symbols

$c$	wave propagation velocity (m/s)
$C_b$	ballast damping (Ns/m)
$C_{rc}$	rail-pad damping of concrete sleeper (Ns/m)

$C_{rw}$	rail-pad damping of wooden sleeper (Ns/m)
$E_{11}$	modulus of elasticity in the fiber direction (GPa)
$E_{22}$	modulus of elasticity in the direction transverse to the fibers (GPa)
$E_{33}$	modulus of elasticity in the direction transverse to the fibers (GPa)
$E_f$	modulus of elasticity of fibres (GPa)
$E_m$	modulus of elasticity of epoxy (GPa)
$f_c$	cutoff frequency (Hz)
$f_{pp}$	pin-pin resonance frequency (Hz)
$f_{pp2}$	2 <sup>nd</sup> order pin-pin resonance frequency (Hz)
$f_r$	rail resonance frequency (Hz)
$f_s$	sleeper anti-resonance frequency (Hz)
$f_t$	full track resonance frequency (Hz)
$G_{12}$	in-plane shear modulus (GPa)
$G_{13}$	in-plane shear modulus (GPa)
$G_{23}$	out of plane shear modulus (GPa)
$G_f$	shear modulus of fibres (GPa)
$G_m$	shear modulus of epoxy (GPa)
$K_b$	ballast stiffness (MN/m)
$K_{rc}$	rail-pad stiffness of concrete sleepers (MN/m)
$K_{rw}$	rail-pad stiffness of wooden sleepers (MN/m)
$V_f$	percentage of fibres (%)
$V_m$	percentage of epoxy (%)
$x$	lateral direction
$y$	vertical direction
$z$	longitudinal direction

# Table of figures

Figure 1.1: a) welded connection [1]    b) jointed connection .....	1
Figure 1.2: Unoccupied track circuit [5] .....	2
Figure 1.3: Occupied track circuit [5] .....	3
Figure 1.4: Exploded view of a 6-bolt IRJ assembly [6] .....	3
Figure 1.5: Broken fishplate [13] .....	4
Figure 1.7: Debonding of the insulation layer [7] .....	5
Figure 1.6: Debonding of end post layer [13] .....	5
Figure 1.8: Crushed end post and metal flow [13] .....	5
Figure 1.9: Broken rail in the vicinity of IRJ [13] .....	5
Figure 1.10: Percentages of IRJ failures (Data from [14]) .....	5
Figure 1.11: Derailment accident due to malfunction of an IRJ, January 2018, Milan [15] .....	6
Figure 1.12: Broken rail in the vicinity of the IRJ, January 2018, Milan [15] .....	6
Figure 1.13: a) NRG-joint,    b) ES joint .....	7
Figure 2.1: Full track resonance [27] .....	12
Figure 2.2: Sleeper anti-resonance [26] .....	13
Figure 2.3: Rail resonance [26] .....	13
Figure 2.4: 1 <sup>st</sup> order pinned-pinned resonance [26] .....	13
Figure 2.5: 2 <sup>nd</sup> order pinned-pinned resonance [26] .....	14
Figure 2.6: a) big hammer    b) small hammer .....	14
Figure 2.7: Averaged hammer force .....	15
Figure 2.8: Averaged acceleration .....	16
Figure 2.9: FRF in accelerance format .....	17
Figure 2.10: Laminate assembly with different fibre orientation [16] .....	20
Figure 3.1: Field measurements location [43] .....	22
Figure 3.2: Measurements location with the traffic direction of the two tracks .....	23
Figure 3.3: Distribution of the accelerometers along the track (red), bolt number (black) .....	24
Figure 3.4: a) small hammer    b) big hammer .....	25
Figure 3.5: Measured sleeper distances (red: larger than 60cm, green: lower than 60cm) .....	26
Figure 3.6: Direct FRF for rail 1.    a) position 1,4    b) position 2,5    c) position 3,6 .....	26
Figure 3.7: Direct FRF for rail 2.    a) position 1,4    b) position 2,5    c) position 3,6 .....	27
Figure 3.8: Direct FRF for rail 3.    a) position 1,4    b) position 2,5    c) position 3,6 .....	27
Figure 3.9: Direct FRF for rail 4.    a) position 1,4    b) position 2,5    c) position 3,6 .....	27
Figure 3.10: Comparison of FRFs for NRG and normal joint - track 1.    a) hit1,4    b) hit2,5    c) hit3,6 ..	28
Figure 3.11: Comparison of FRFs for NRG and normal joint - track 2.    a) hit1,4    b) hit2,5    c) hit3,6 ..	28
Figure 4.1: Sketching of rail, insulation layer and fishplate .....	29
Figure 4.2: Hammer force .....	32
Figure 4.3: FE model of the NRG joint .....	37
Figure 4.4: FE model of the normal joint .....	37
Figure 4.5: Direct FRF for the NRG-joint.    a) hit1,4    b) hit 2,5    c) hit 3,6 .....	39
Figure 4.6: Direct FRF for the normal joint.    a) hit1,4    b) hit 2,5    c) hit 3,6 .....	39
Figure 4.7: Accelerance function with varying vertical damping for ballast .....	40
Figure 4.8: Accelerance function with varying vertical stiffness for ballast .....	40
Figure 4.9: Accelerance function with varying vertical damping for rail-pads .....	41
Figure 4.10: Accelerance function with varying vertical stiffness for rail-pads .....	41
Figure 4.11: Validation of transfer accelerances for the NRG-joint .....	42
Figure 4.12: Validation of transfer accelerances for the normal joint .....	43
Figure 5.1: 1 <sup>st</sup> order pinned-pinned resonance .....	44
Figure 5.2: Sleeper distribution in the two sides of the joint (cm) .....	45
Figure 5.3: Comparison between uniform and non-uniform sleeper span. Case 1 .....	45

Figure 5.4: Comparison between uniform and non-uniform sleeper span. Case 2 ..... 46  
Figure 5.5: Comparison between uniform and non-uniform sleeper span. Case 3 ..... 46

# 1. Introduction

## 1.1 General

Rail transport is one of the most dominant means of transport worldwide. Train is the fastest, safest and most comfortable transport choice compared with any other land transport [1]. It can carry huge numbers of passengers or extensive cargo loads at high speed in one unit, while the same amount or burden would take numerous buses, lorries or cars. Rail transport also mitigates the environmental pollution by reducing CO<sub>2</sub> emissions because it is significantly more energy efficient than road or air transport.

Especially in the Netherlands, the rail transport/infrastructure is “the backbone of the public transport system”. 1,1 million people use the train every day, due to the numerous benefits (e.g. free of road traffic, safety). Rail transport in the Netherlands uses a dense railway network that connects virtually all major towns and cities, counting as many train stations as the municipalities in the Netherlands [2].

All these advantages of rail transport make it more and more attractive choice but at the same time the demands (passengers demand for shorter travel times and freight transport for higher capacities) increase. These demands may cause the railway system to reach its operational and structural strength limits[3]. Numerous measures need to be taken, to ensure that all the track components satisfy the requirements, regarding these limits. This thesis examines the behaviour of one of the most important components in railway track -- the insulated rail joint (IRJ), whose function is described in the next section.

## 1.2 Function of the IRJ

There are two main types of rail connection in modern railway engineering: a. continuous welded rails (CWRs) and b. insulated rail joints (IRJs) (figure1.1).



Figure 1.1: a) welded connection [1] b) jointed connection

IRJs serve two critical purposes in railroads. They act as a barrier to electrical currents, allowing the rails on each side of the joint to form separate electrical circuits (track circuits) and they enable detection of broken rails. Electrical insulation of the rails in an IRJ configuration is carried out by breaking the continuity of the steel and replacing it with various insulating materials while maintaining the structural integrity of the rail track.

Most railway tracks use track circuits to identify which sections of track are occupied by trains. The closed circuit track circuit was patented by Dr. William Robinson in 1872 and allowed for automatic block signalling to be implemented [4].

To make the system work, tracks are partitioned into blocks of varying length. Each block is separated from the neighbouring blocks by an insulated joint between rails. Blocks are monitored by electrical equipment to control train movements. Signals are transmitted to the cab of the train and are not present next to the tracks except at switches. Each block has a track circuit which identifies if a train is present.

Track circuits work by running a circuit using the rails to connect a power source at one end of the block with a relay at the other end. The relay and power source are connected to each rail by cables. As long as the circuit is complete, low voltage power flows down one rail, through a relay, and returns to the power source via the other rail. If the circuit is complete, the relay will be energised, which keeps signals in the “clear” position. If the circuit is broken, the system fails in a safe manner. A broken rail or a failed power source causes the relay to become de-energised and report the section of track as occupied.

Figures 1.2 and 1.3 illustrate how this system works:

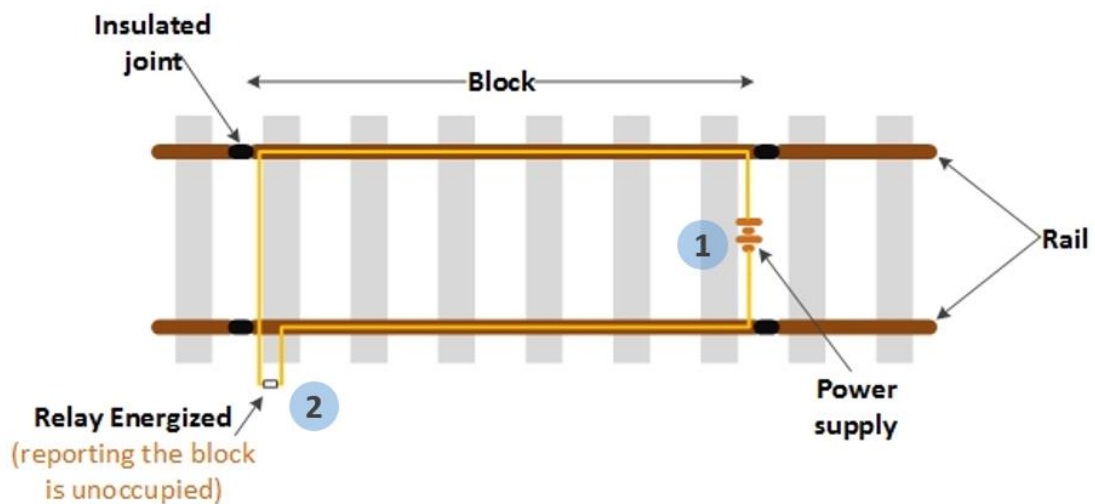


Figure 1.2: Unoccupied track circuit [5]

**Unoccupied Track Circuit (green):** The completed circuit is shown in yellow in figure 1.2. The power source located at number “1”, while the relay is located at number “2”.

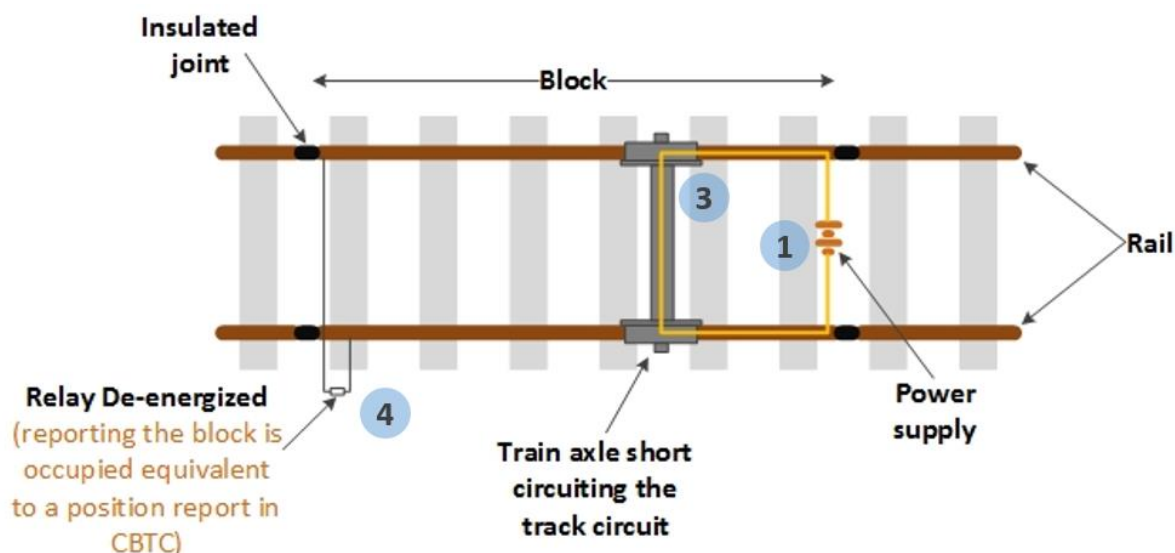


Figure 1.3: Occupied track circuit [5]

**Occupied Track Circuit (red):** A train is detected when it shorts the circuit. In railroading, this is called “shunting” the circuit. Once the train enters a block, the metal wheelset conducts the circuit as a short cut that bypasses the relay. This de-energises the relay, which causes signals to report the block as occupied. This can be seen in figure 1.3: “1” indicates the power source, “3” denotes the wheelset of the train which shorts the circuit, and “4” represents the de-energised relay.

The IRJ consists of an insulating layer (e.g. fiberglass) with an adhesive (e.g. epoxy), which is placed between the rail and the fishplates. The insulating end-post is used to insulate the rail ends from each other, and is most of the times produced from nylon, epoxy fibre-glass laminated sheet or polyurethane. In addition, the insulating layer, the bolts and the washers are fully covered with adhesive to prevent voids in the completed joint. A typical IRJ assembly is shown in figure 1.4.

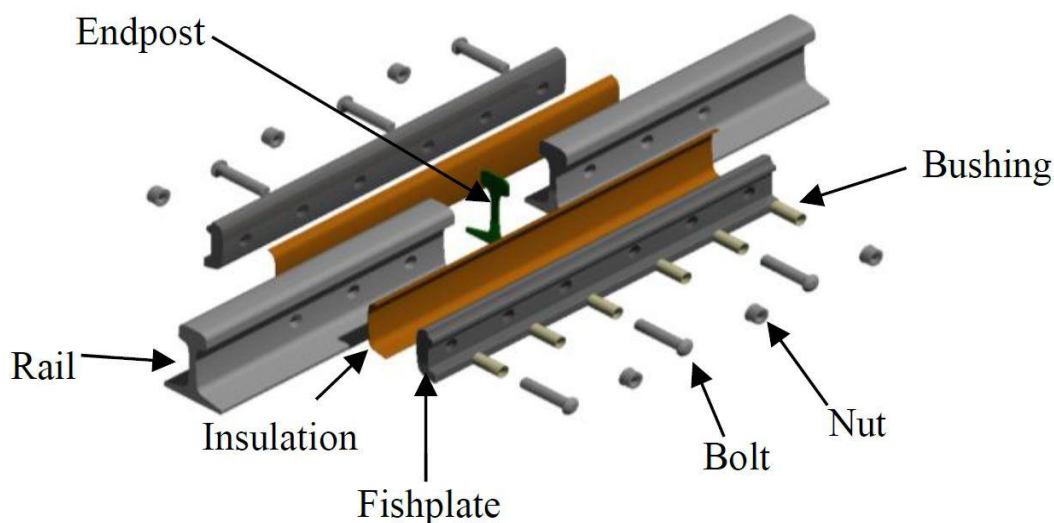


Figure 1.4: Exploded view of a 6-bolt IRJ assembly [6]

### 1.3 Problem statement

Railway track performs best when there is a smooth uniform interface between the wheels and the rail. Any local irregularity in the running surface stimulates the train-track interaction system, generating high impact forces that may damage the wheels and / or the track. For more than a century, the most common discontinuity in the running surface of the rail was the rail joint [7]. Despite the significance and the frequent use of the IRJs, their service life is still quite low. IRJs are still characterized as areas of high vulnerability for traffic and high damage potential for the track. On lines with heavy axle loads and high tonnage, IRJs have shorter service lives than any other track component except high-angle crossing diamonds [8]. The discontinuity due to the change of geometry and, more important, due to the change of stiffness gives rise to high dynamic loads, which accelerate the mechanical failure. Consequently, IRJs routinely fail after carrying about 50 million gross tonnes of freight traffic (approximately 1-2 years). This results in significant maintenance costs for the rail industry and service interruptions due to accidents around the world [9-12]. To improve the design of IRJs, understanding of their failure modes is first necessary. There are two types of failure that occur in IRJs: electrical failure and mechanical failure. Electrical failure is caused when the electrical isolation between the two connected rails is lost and can be caused either by mechanical failure or by other factors such as lipping and contamination. Based on various designs of IRJs worldwide, common mechanical failure modes of the IRJS, include:

- Cracked fishplates, usually initiated at the bolt holes (figure 1.5)
- Debonding of the end post insulating layer from the rail ends (figure 1.6)
- Debonding of the insulating layer between the rails and the fishplates (figure 1.7)
- Crushed end post and metal flow (figure 1.8)
- Broken rail in the vicinity of the IRJ (figure 1.9)
- Macro-scale dipping of the insulating joint due to settling of the supporting sleepers, and also plastic deformation of the rail edge at the insulating layer.



Figure 1.5: Broken fishplate [13]



Figure 1.7: Debonding of end post layer [13]



Figure 1.6: Debonding of the insulation layer [7]



Figure 1.9: Crushed end post and metal flow [13]



Figure 1.8: Broken rail in the vicinity of IRJ [13]

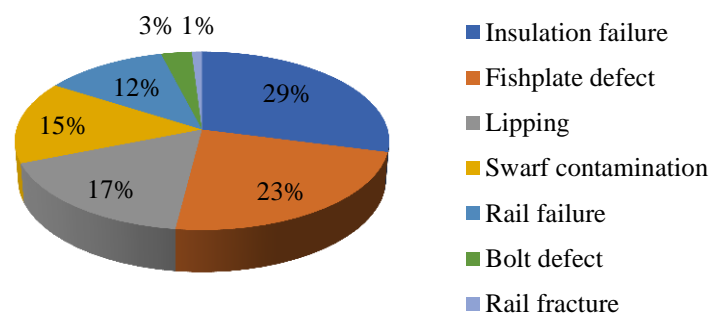


Figure 1.10: Percentages of IRJ failures (Data from [14])

Figure 1.10 illustrates the main reasons of IRJ failure and their percentages.

All these problems may lead to disturbances of rail operation and high maintenance costs, and, in the worst case fatal accidents. An example can be seen in figures 1.11 and 1.12:



*Figure 1.11: Derailment accident due to malfunction of an IRJ, January 2018, Milan [15]*

Figure 1.11 shows an accident that happened at 25 January 2018, after the derailment of a train which was heading to Milan. The accident caused the death of 4 people and also many serious injuries. The derailment was due to the malfunction of an IRJ (figure 1.12).



*Figure 1.12: Broken rail in the vicinity of the IRJ, January 2018, Milan [15]*

This accident clearly indicates that, even today, the failure of IRJs remains a worldwide problem in railway networks, which requires further investigation and improvement.

## 1.4 Research objective

The objective of this M.Sc. thesis is to investigate and optimise the dynamic behaviour of the IRJ. Two joint types are examined, which are used in the Dutch railway network, the NRG-joint (figure 1.13a) and the normal joint<sup>1</sup> (figure 1.13b). As a new type of joint, the NRG-joint is gradually replacing<sup>2</sup> the normal joint in the Dutch railway network (only in straight track).



Figure 1.13: a) NRG-joint, b) ES joint

The following questions are answered in this thesis to achieve the research objective:

### 1. How do the NRG-joint and the normal joint respond to the hammer excitation?

This new joint has only been tested using static tests (4-point bending test, tension test), but these tests fail to present its dynamic behaviour. Conducting dynamic measurements can help us to identify its dynamic behaviour.

### 2. Does the NRG-joint behave better than the normal joint?

The purpose of the NRG-joint is to replace the normal joint, so it is of great importance to know if the new joint behaves better than the normal one. By analysing the Frequency Response Function (FRF), the amplitude of vibrations for both joints can be identified, and further used as measure to compare their behaviour.

### 3. Which parameters affect the dynamic behaviour of the NRG-joint and the normal joint?

It is also crucial to identify which parameters affect the dynamic behaviour of this joint, as well as the way that they affect it.

<sup>1</sup> Normal joint is defined as the four-bolt IRJ used until now in the Dutch railways

<sup>2</sup> The NRG-joint has been implemented in the Dutch railways since 1<sup>st</sup> October 2016

#### 4. How can the performance of the NRG-joint and the normal joint be optimised?

Section 1.3 shows clearly that the performance of IRJs is not perfect, therefore, there is space for improvement. Using field measurements observations and numerical models in order to identify the parameters that affect the design, the behaviour of the joint can be improved.

### 1.5 Novelty of this research

The main novelty of this research is the proposed optimisation strategy to reduce certain resonances of IRJs. By analysing the measurement results it was found out that the sleeper span influences the dynamic behaviour of the IRJ. Then, using the numerical model to reproduce the measurements and perform a parametric analysis, a new design which is expected to improve the dynamic behaviour of the system, has been proposed.

Another novelty of this thesis is the implementation of the insulation layer. Many numerical models have been developed in order to study the behaviour of the IRJ. However, in these models the insulation layer between the fishplate and the rail is omitted. That is mainly because the insulation layer is a composite material whose mechanical properties depend on many factors (e.g. percentage of fibres, fibres orientation etc.) and can hardly be modelled. In this thesis, this insulation layer has been included in the IRJ model to make the model more complete (more parts of the IRJ track structure are included).

### 1.6 Overall approach

The approach used in this thesis consists of three main parts, as follows: The first part is the numerical (FE) modelling. Two FE IRJ models are developed, to describe the behaviour of the actual tracks in the field as realistically as possible. Hammer tests are then reproduced with the FE IRJ models to study the dynamic behaviour of the IRJs numerically. The second part consists of field measurements (hammer test) which are used, first to investigate the dynamic behaviour of the IRJs experimentally and second to calibrate and validate the FE model. In the last part, the validated model from the first two parts, is used to conduct a sensitivity analysis in order to improve the dynamic behaviour of the studied IRJ.

### 1.7 Assumptions and limitations

In order to reduce the complexity of the problem, the rail-pads and the ballast were simulated as systems of springs and damper elements. This leads to limitations due to the nature of the elements employed. In addition, only the response in the vertical direction was considered, while the response in the lateral and longitudinal directions were not taken into account. The insulation layer between the fishplates and the rails was assumed to be a typical fibre-glass epoxy material, as no mechanical testing was possible for this material. The exact values of

the mechanical properties of this material (Young's modulus, Poisson's ratio, shear modulus) were not available, so a formula ("rule of mixtures") that calculates these values was used. The fibres of this material were assumed to be uni-directional in the vertical direction. The percentage of the fibres was assumed to be 55% which is a typical value from literature review[16]. In addition, the bolts were simulated as pressing forces.

## 1.8 Structure of this thesis

This thesis is divided into 6 chapters as follows: In Chapter 2 the necessary literature study is presented concerning research approaches that have been used in order to investigate the behaviour and the causes of failure of the IRJs. It also provides the necessary theoretical background regarding the dynamics of the system and previous attempts to optimise the system behaviour. In chapter 3 the procedure of the field measurements is described, as well as measurements observations are discussed. In Chapter 4 the problem is modelled using a three-dimensional (3D) FE model, and an implicit-explicit dynamic analysis is conducted in order to identify the dynamic characteristics of the system and the resonance frequencies. The used elements, material models, constrains and the simulation techniques are also explained in this chapter; in addition, the FE model is calibrated and validated with the measurements. The results from the measurements and the numerical simulations are compared with previous studies. In chapter 5 parametric study is carried out to assess the influence of sleeper distribution on the dynamic behaviour of IRJs, and the optimisation strategy is proposed. Finally, in chapter 6, all the conclusions of the present research are presented, and some recommendations are given for further investigation. Appendix A contains detail description of the elements that were used in the FE model. Appendix B describes the augmented Lagrange Method.

## 2. Background & Literature review

*In this chapter an extensive research regarding the previous models that used to tackle the problem of IRJs and the necessary scientific background are presented.*

### 2.1 Previous models

Many researchers have studied the static and dynamic behaviour of the IRJ using analytical and numerical solutions.

Kerr and Cox studied the problem of IRJ as a structural “weak spot” in the track [17]. In their model, which was solved analytically, they calculate the deflection of a bonded IRJ under vertical loads, using three beams (two semi-infinite beams to represent the rails and one beam to represent pair of joint bars) connected by vertical Winkler-type springs (to represent epoxy fiberglass layers), whose stiffness was calibrated by a static load measurement. Their model is primarily applicable to scenarios characterised by a slow-moving railway traffic load.

Suzuki et al [18] measured parameters related to the track dynamic behaviour, such as dynamic wheel loads and rail seat forces near a rail joint produced by running vehicles. They also proposed a track dynamic model for rail joints to account for the excitation by the running wheel. The comparison between the measured and analytical results showed a good agreement. Finally, they proposed a predictive model of ballast settlement near rail joints and calculated the effects of countermeasures against joint dips on ballast settlement.

Wu and Thompson (2003) represented the joint in their model as a pin between two semi-infinite Timoshenko beams and calculated the wheel-IRJ interaction by a relative displacement excitation model proposed by Grassie et al. (1982). Kitagawa et al. revised Wu and Thompson’s model by changing the pin with a complex spring to represent the joint, whose vibratory behaviour level was validated against a field test [19].

With the development of more powerful computers which can handle faster complex calculations, the use of numerical models (e.g. FEM models) has been increased. FEM is a useful tool to evaluate the behaviour of the IRJ (e.g. maximum bending stresses, contact stresses, response to impact loading) under operational loading conditions and identify possible areas of failure. Results from previous FEM studies regarding the IRJ are presented and discussed in table 2.1. In all the presented models the static behaviour of the IRJ is studied, while little attention has been paid until now in FEM models which consider the dynamic behaviour of the IRJ.

Author	Research topic	Modelling technique	Comments
Talamini et al [20]	Fatigue estimation of fishplates	Static 3D FEA in ABAQUS, under vertical load, six bolted RJ.	A 3D static model of a mechanical RJ including elastic support conditions under a vertical load increased by a dynamic load factor is used to estimate the bending and reverse bending stresses on fishplates. A fatigue life estimation of the fishplates is proposed using Miners's Law. A comparison is made between FEA results and theoretical stress calculations using the beam theory and thermal stresses. The study suggests the 3D FEA can provide a better understanding of a biaxial bending behaviour of fishplates that is critical for fatigue calculations which cannot be predicted by beam theory.
Himebaugh et al. [21]	FEA of bonded IRJ	Static 3D FEA of supported IRJ in ABAQUS	One type of supported bonded IRJ. Model included a fishplate of length 1.2 m, no rigid bolts modelled, wooden sleepers and elastic foundation. A model length of 7.6m was considered sufficient to model on each side of the wheel after parametric analysis. Effect of thickness and length of joint bar, load position and size of sleepers on rail deflection and epoxy stresses are investigated under vertical 145 kN and tensile 1330 kN load in the rail.
Mandal, Mandal and Dhanasekar [22]	Plastic deformation of railhead in IRJ	3D FEA, ABAQUS, plastic deformation of railhead, non-linear isotropic and kinematic material hardening model for 2000 cycles	Six-bolt suspended IRJ, account for bolt pre-tension 200 kN. 700mm spacing, 3D part 2.4 m, 9.6m in 1D. 174 kN wheel load. Too low vertical displacement (0.2 mm). Sleepers fixed with zero degrees-of-freedom not representative of field conditions in contrast with the authors' model. Model representative of a laboratory experiment of rail joint. The plastic zone of the top surface of rail head material is investigated
Ding and Dhanasekar [23]	Flexural behaviour of bonded-bolted butt joints due to bolt looseness	ABAQUS 3D FEA, pre-stressing of bolts, in-plane bending in bolted IRJ.	Elasto-plastic material law for fishplates only, elastic law for the rest. Bonded connections among rail–fishplates–bolts, bolt preload are accounted. Effect of looseness of bolts under biaxial stress on the RJ.
Sandstrom and Ekberg [24]	Fatigue impact and plastic deformation of IRJ	3D FEA of IRJ, wheel rail contact, non-linear kinematic hardening constitutive model	The model indicates that the main failure mechanism of IRJs is ratcheting and not the low cycle fatigue. Model included only a part of the wheel, railhead edges and endpost. Effect of increase of frictional coefficient between rail and wheel, increase of endpost thickness and effect of rail edge bevelling under multiaxial loading conditions on the total accumulated plastic strain in rail are investigated.
Bandula-Heva and Dhanasekar [25]	Localised plastic strain accumulation in railhead edge	3D FEA of railhead edge using Caboche kinematic hardening law using experimental uniaxial monotonic tension tests of railhead coupons.	FE validated model is used to predict localised plastic strain in railhead edge.
Mandal and Peach [26]	FEA of IRJ	Static 3D FEA of a six-bolt IRJ, with an objective to investigate the effect of fishplate width on stresses in railhead.	Fixed support on rail bottom, the rail was tied to the sleepers, no interaction between rail and fishplate, welded joint. The effect of fishplate width in stresses on railhead and in deflection was investigated. Too stiff conditions indicated very low deflection results.

Table 2.1: Previous studies regarding FEM analyses in IRJs

## 2.2 Vertical track dynamics

The dynamic behaviour of the track can be divided into three groups depending on the vibration frequency of the mode (table 2.2) according to [27]. In the low frequency range (0-40Hz), the substructure layer plays the dominant role to the track response. For the middle frequency range (40-400 Hz), the sleepers and ballast are the two parameters which dominate the track response. For the high frequency range (400-3000 Hz), mainly the superstructure layer affects the track response. The middle and high frequency track dynamics are illustrated in the following subsection.

Frequency (Hz)	Range
0-40	Low
40-400	Middle
400-3000	High

Table 2.2: Frequency ranges for track vibrations

### 2.2.1 Vibration of the track (40Hz-400Hz)

Two types of the track vibration modes can be identified in in the mid-frequency range (40Hz to 400Hz).

*Full track resonance ( $f_t$ ):* The lowest possible vertical resonant frequency of the track is the full track resonance. In this mode all the components of the track vibrate and the structure bends as a whole (figure 2.1). This mode is observed when the system vibrates in frequencies between 40Hz and 140Hz. The ballast properties (e.g. stiffness and damping) determine the full track resonant frequencies.

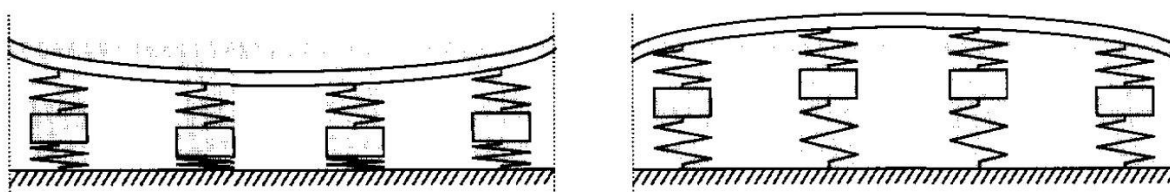


Figure 2.1: Full track resonance [27]

*Sleeper anti-resonance ( $f_s$ ):* In the second vertical resonant frequency, the sleepers of the track have large vertical movement, while the rail stays static (figure 2.2). This mode is called the sleeper anti-resonant mode and it is observed in frequencies between 100Hz and 400Hz. This mode is affected by the sleeper properties such as its mass, as well as the stiffness of the rail-pad and ballast.

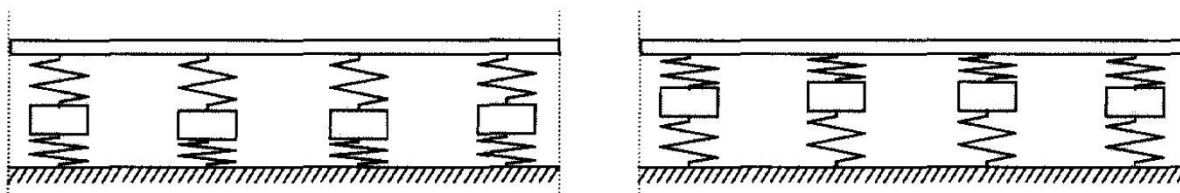


Figure 2.2: Sleeper anti-resonance [27]

### 2.2.2 Vibration of the rail (400Hz-3000Hz)

Three types of vibration modes can be identified in the high-frequency range (400Hz to 3000Hz), namely:

*Rail resonance* ( $f_r$ ): The first high frequency vibration mode is the rail vibration. In this mode, the rail vibrates relative to the supports, while the other components of the track show small or no movement (figure 2.3). This mode highly depends on the rail-pad properties and its frequency range is between 500Hz and 1100Hz.

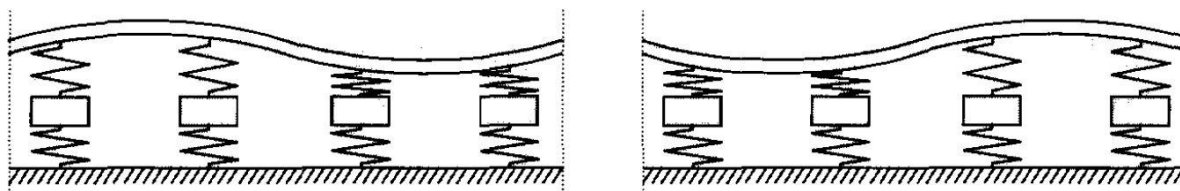


Figure 2.3: Rail resonance [27]

*Pinned-pinned resonance* ( $f_{pp}$ ): The second high frequency mode of the rail vibration is known as pinned-pinned resonance. In this mode the rail vibrates with its nodes on the sleepers (figure 2.4). It occurs when the wavelength is twice the sleepers spacing. It is observed in frequencies between 800Hz and 1200Hz. The distance of the sleepers influences greatly this type of mode.

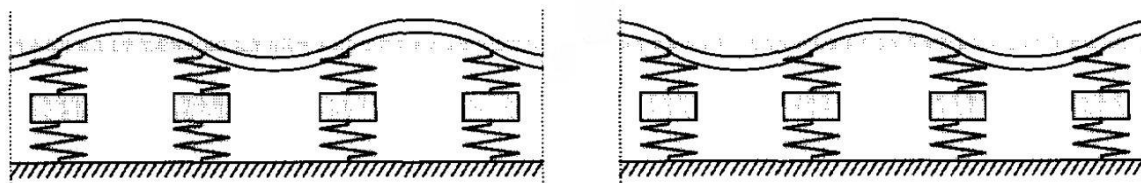


Figure 2.4: 1<sup>st</sup> order pinned-pinned resonance [27]

*Second order pinned-pinned resonance ( $f_{pp2}$ ):* The rail vibrates with its nodes on the sleeper at half wavelength of the pinned-pinned resonance (figure 2.5). Same as the first order pinned-pinned resonance, the distance of the sleepers determines the frequency and its characteristics. This mode is observed generally between 2600Hz and 3000Hz.

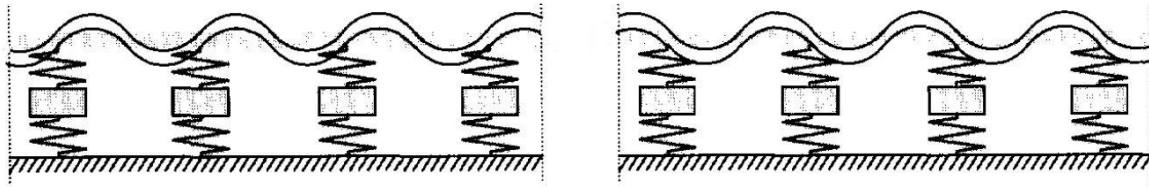


Figure 2.5: 2<sup>nd</sup> order pinned-pinned resonance [27]

### 2.3 Identifying track dynamics using hammer tests

Hammer test is a widespread non-destructive test (NDT) in railway engineering used to identify the track dynamics [3], [28]. In this test the track is excited by an impulse force and the response is measured at the points of interest. In order to obtain meaningful testing results, the hammer tests should be conducted at nominal locations. Depending on the frequency range of interest, different hammer weights and tips are used [3]. For low frequencies heavy hammers with soft plastic tips are widely used, while light hammers with hard tips are more often used to excite high frequency vibrations (figure 2.6). For the superstructure layer, the vertical dynamics of the track is of main concern, so the hammer tests are generally performed by exciting the rail top in the vertical direction, either on a rail section located on the sleeper support (on-support configuration) or on a rail section in the middle of two sleeper supports (mid-span configuration); the vertical vibration response of the track is then collected. To minimize the random error the rail can be excited multiple times at every point of interest and then the average input (force) and output (acceleration) are calculated (figure 2.7, 2.8). The post processing of the results includes transforming of the measured time-domain signals into the frequency domain, filtering signals (e.g. low-pass filtering), and calculating the FRF (figure 2.9).



Figure 2.6: a) big hammer b) small hammer

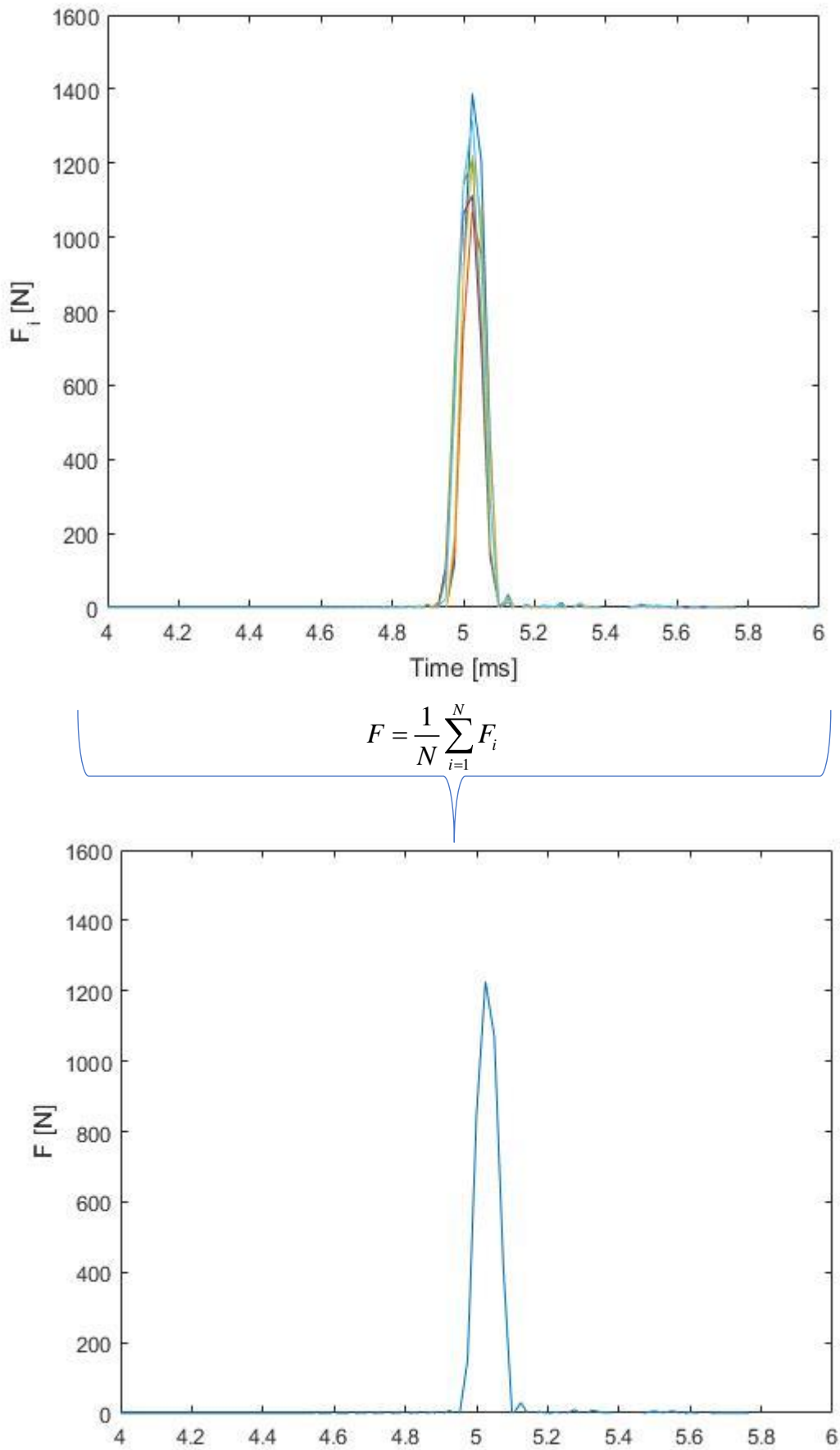


Figure 2.7: Averaged hammer force

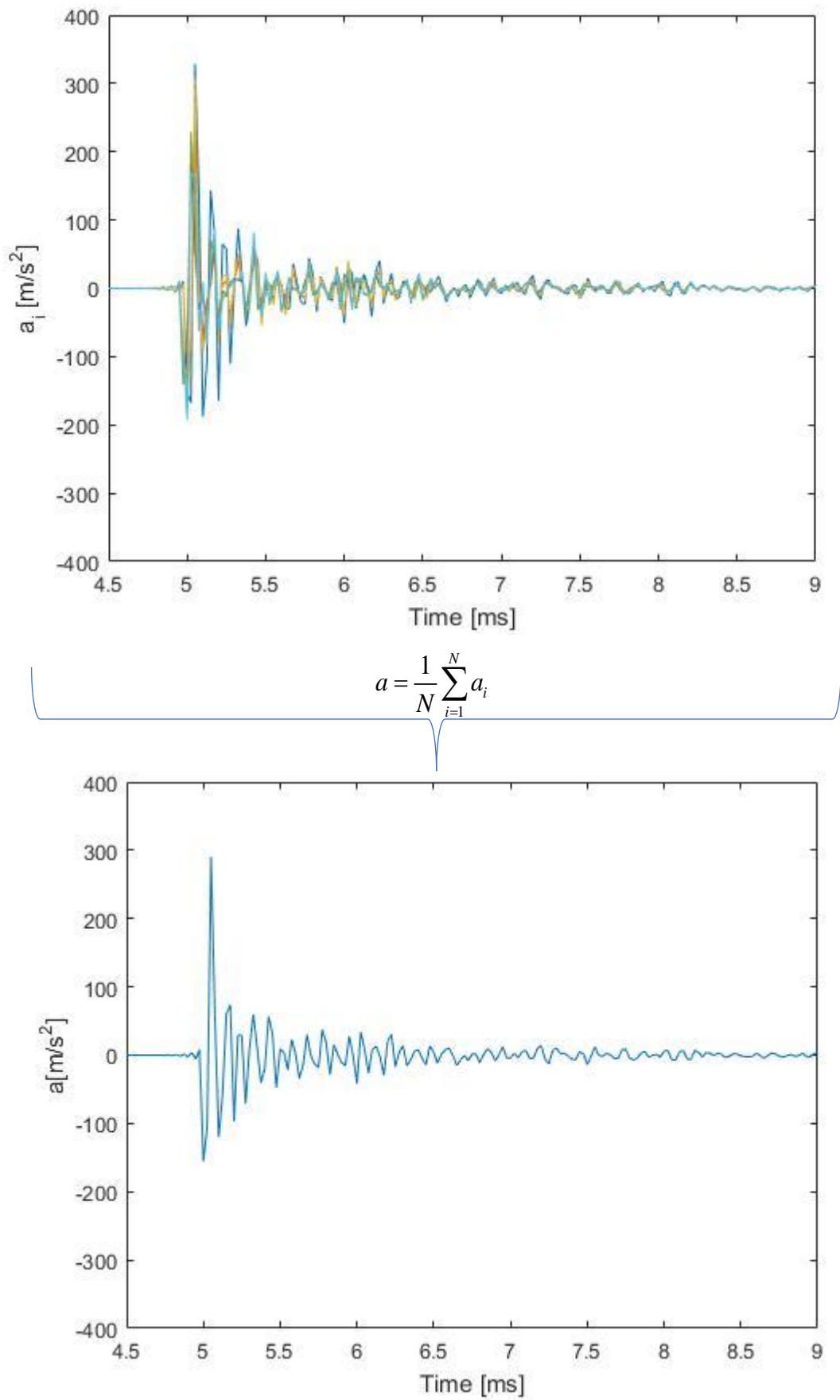


Figure 2.8: Averaged acceleration

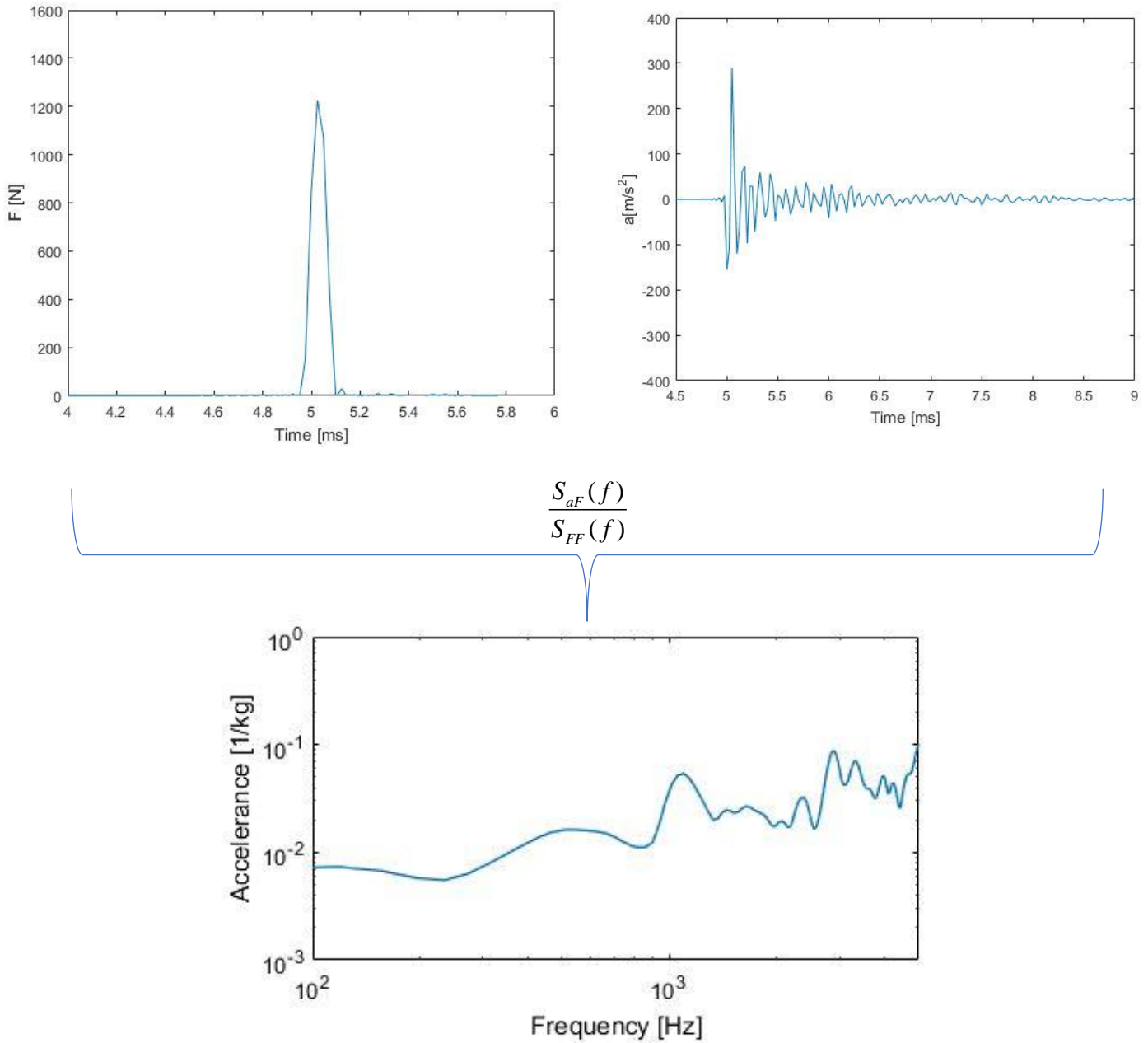


Figure 2.9: FRF in acceleration format

where  $S_{aF}$ =complex cross-spectrum of acceleration  $[\text{mN/s}^3]$

$S_{FF}$ =power spectrum of force  $[\text{N}^2/\text{s}]$

Hammer test is a simple and inexpensive measurement system. Valuable information about the track dynamic behaviour can be obtained. The analysis of hammer test gives an insight into the dynamic behaviour of tracks owing to the obtained FRF. The resonances and anti-resonances of the track occur can be identified with the FRF, shown as peaks and dips, respectively. The knowledge of these may contribute to structural modification, evaluation of the structural integrity and reliability, condition monitoring and model updating. Damping measures can be designed to attenuate vibrations at these frequencies (resonance frequencies), which lead to accelerated deterioration of the track. This study combines the hammer test measurements with numerical modelling so that: a) the characteristic frequencies are identified, b) track parameters that can hardly be measured directly (stiffness and damping of rail-pads and ballast) are derived and c) the numerical models are validated.

Esveld and Amy De Man proposed the use of vibration behaviour of the railway track structure in the mid and high-frequency range that can act as an indicator for the performance of the track structure with respect to the sound radiation, vibration sensitivity and wheel-rail interaction forces [29].

Kaewunruen and Remennikov developed an NDT approach for the dynamic condition of railway track structures combining field measurements and track simulation [30]. Their research proposes an alternative NDT technique to evaluate the integrity of railway track for two specific defects: cracked sleeper and damaged rail fasteners.

Oregui et al. developed an experimental investigation in order to determine the structural condition of the IRJ using the dynamic response from an impact excitation for different damaged states in the rails [31]. The technique shows the potential to monitor and assess the condition of IRJ through an analysis of dynamic responses due to hammer excitation or wheels passing over the gap of IRJ. In addition, Oregui et al., used a (FE) model to simulate a hammer test with the purpose of identifying the dynamic parameters of the track which could help to developed adapted maintenance methods or track design to prevent or avoid defects [32].

Yang et al. investigated the track dynamics and the dynamic behaviour of an IRJ using an explicit FE model and validated the results with hammer tests and pass-by measurements [28]. The effects of the dynamics in the lateral direction are also included in the study.

## 2.4 Influence of sleeper span on the dynamic behaviour of the track

Previous studies have shown that sleeper span can affect the dynamic behaviour and deterioration of the track.

Sadri et al. studied the effect of railway track parameters on the expected degradation of track geometry. In his study, a frequency domain model of a discretely supported rail coupled with a moving unsprung mass is used. The susceptibility of the track to degradation is quantified by calculating the mechanical energy dissipated in the substructure. Three different cases for the sleeper span are considered, namely 0.5m, 0.6m and 0.7m. Among other parameters, sleeper span was found to have a significant effect, with higher expected degradation rates for increasing sleeper span [33].

Zakeri et. al studied the dynamic behaviour of the track using a track-train interaction model. In this model a sensitivity analysis is carried out, to identify which parameters affect the deterioration of the track elements. From the results it is concluded that reducing sleeper span increases the variation of the overall track stiffness and hence reduces all of the track responses and interactive forces [34].

## 2.5 Optimisation of the behaviour of IRJ

Matching the service life of an IRJ to continuously welded rail has been the underlying goal of many research and design studies. Numerous researchers tried to optimise the behaviour of the IRJ by modifying the initial design.

K. Mandal investigated the change in the stress state of an IRJ by changing the end post material (a. Fiberglass epoxy, b. Nylon PA 66, c. PTFE) and the joint bar thickness (a. 30mm, b. 34mm, c.40mm) under the application of a static load of 180 kN [26].

M. Galou proposed an alternative to reduce the deterioration and failure of the IRJ by external reinforcement using strap rails or more robust I-beam sections in the vicinity of the IRJ [6].

M. Akhtar et al investigated the change in the response, after modifying a number of parameters in the IRJ design, and namely the modulus of the fishplates, the adhesive material and the insulator material and proposed a new design with a diagonal cut which allows smooth transition of wheels from one rail to another and lowers adhesive and joint bar stresses significantly [35].

An extensive research for the optimisation of IRJs was conducted by N. Zong in his/her PhD thesis [14]. The researcher developed two new designs regarding the structure of the IRJ

which showed promising results. The first proposal concerns shape optimisation of the railhead at the rail end by changing the original sharp corner into an arc profile in the longitudinal direction, in order to reduce the stress singularities. To eliminate the problem of bolt hole cracking and joint bar cracking he also proposed another conceptual design in which the rails are embedded into the concrete post tensioned sleepers.

In this MSc thesis a new design with non-uniform sleeper span distribution is proposed, aiming to improve the dynamic response of the IRJ.

## 2.6 Fibre-reinforced plastics

According to [17], [36-40], the insulation layer between the rail and the fishplates consists, most of the times, of fiberglass epoxy which is a special category of FRPs (Fibre-reinforced plastics).

Fibre-reinforced polymers (FRP) are a type of composite material that combine layers of very small ( $\text{Ø}=12\mu\text{m}$  [41]) but high strength fibres with a viscous resin matrix (e.g. epoxy); upon curing of the viscous matrix a unique composite material is born with highly desirable properties. There are a number of materials that can make up an FRP composite, with a range of resin and fibre types that yield different properties upon combination. However, most of them possess high strength to weight and corrosion resistance attributes. There are also a number of production techniques each with their own circumstantial advantages and disadvantages.

Fibres can be made from a range of materials, including glass, carbon and aramid and generally have a very high tensile strength in the longitudinal direction (carbon fibres up to 7GPa [16]). Glass fibres are the most commonly used in civil engineering applications due to their low cost ( $\sim\text{€}2/\text{kg}$  [16]). Fibres are very anisotropic, meaning that in order to create a suitable, structural material fibres must be placed in different alignments to provide strength in various directions. Figure 2.9 shows the creation of a laminate where unidirectional fibres are placed in plies at different angles to create a material with load carrying ability in each of the directions.

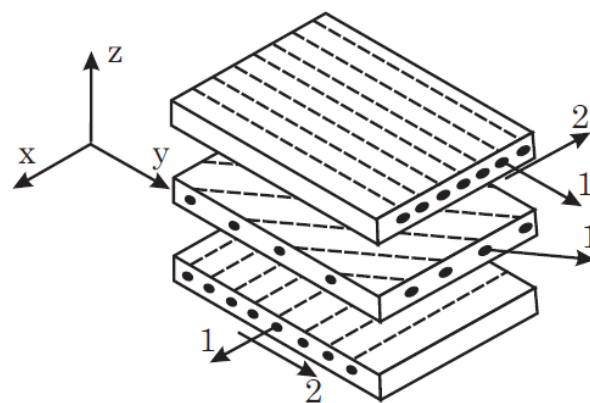


Figure 2.10: Laminate assembly with different fibre orientation [16]

While the fibres give the material most of their strength, the resin also performs a key role in bonding the fibres together. This bond restrains the fibres from buckling under compressive load; due to the very small size of the dry fibres they can buckle very easily under minimal load if they are not restrained. The resin also provides environmental protection to the fibres, which is leading to FRP becoming a serious competitor to steel and reinforced concrete in the infrastructure sector, due to lower levels of maintenance required for bridges [16].

Due to the high strength of the fibres the material has a high strength to weight ratio, which is beneficial in a number of applications. For this reason, many new applications which benefit from high strength, low weight structures have adopted FRP ahead of traditional materials or new-age metal alloys. Other benefits over conventional materials like steel and concrete include: more favourable fatigue behaviour, pre-fabrication possibilities and the ability to design the strengths in each direction.

Continued research and development from early adopters have led to refined manufacturing and production techniques that paved the way for a range of markets, such as: cryogenics, sports equipment and the aerospace and naval industries.

However, FRP is not without its limitations. Due to the relatively low stiffness of the material, when compared with traditional construction materials like steel, serviceability criteria govern many FRP designs. FRP does not have the ability to deform plastically and hence exhibits a brittle failure mode, this means that it struggles to continue to provide structural performance after impact damages.

## 3. Field measurements

*In this chapter the procedure of the measurements is explained. The tests performed in field measure the vibration response of the rails using two instrumented hammers (small hammer and big hammer), depending on the desired frequency range to be measured. Using the measurement data, the difference in the behaviour between the normal and NRG-joint is also evaluated. The excitations are conducted, and the response are measured at multiple points of interest. The measured IRJs are considered to be in healthy conditions. The measurements were conducted on Sunday 10<sup>th</sup> of June 2018.*

### 3.1 Location

The location where the field tests were performed is on the track line between Zwolle and Meppel (at km75.9 by signals 505 and 507), in the Meppel–Groningen railway line. The Meppel–Groningen railway is an important railway line in the Netherlands running from Meppel to Groningen, passing through Hoozevee and Assen. The line was opened in 1870. It is also known as the *Staatslijn "C"* [42].



Figure 3.1: Field measurements location [43]

## 3.2 Track site

As it can be seen from figures 3.1, and 3.2 below, the measured joints are close to the start of a turn near Marsweg but they are in straight track. The traffic at the track site is one-directional (see figure 3.2). In Rail1 and Rail3 the NRG-joint is installed, while in Rail2 and Rail4 the normal joint is installed. In the track, UIC54 rails with inclination 1/40 are supported by NS90 sleepers every 0.6m except in the vicinity of the IRJs. The IRJs are supported with double wooden sleepers to reduce the deflection of the joint. Furthermore, the wooden sleepers introduce damping to the system, which helps in the absorption of vibrations caused by the impact when a wheel rolls over the discontinuity of the IRJ. In both tracks an NRG-joint and a normal joint are installed (see figure 3.2). In track 1, the train heads to Zwolle station, while in track 2, the train goes to the opposite direction. For track 1 the NRG-joint was installed in January 2018. For the normal joint there is no information available about when it was installed on the track. For track 2 the NRG-joint was installed in February 2018 and the normal joint was in 2017. In this study all four joints have been examined and analysed.

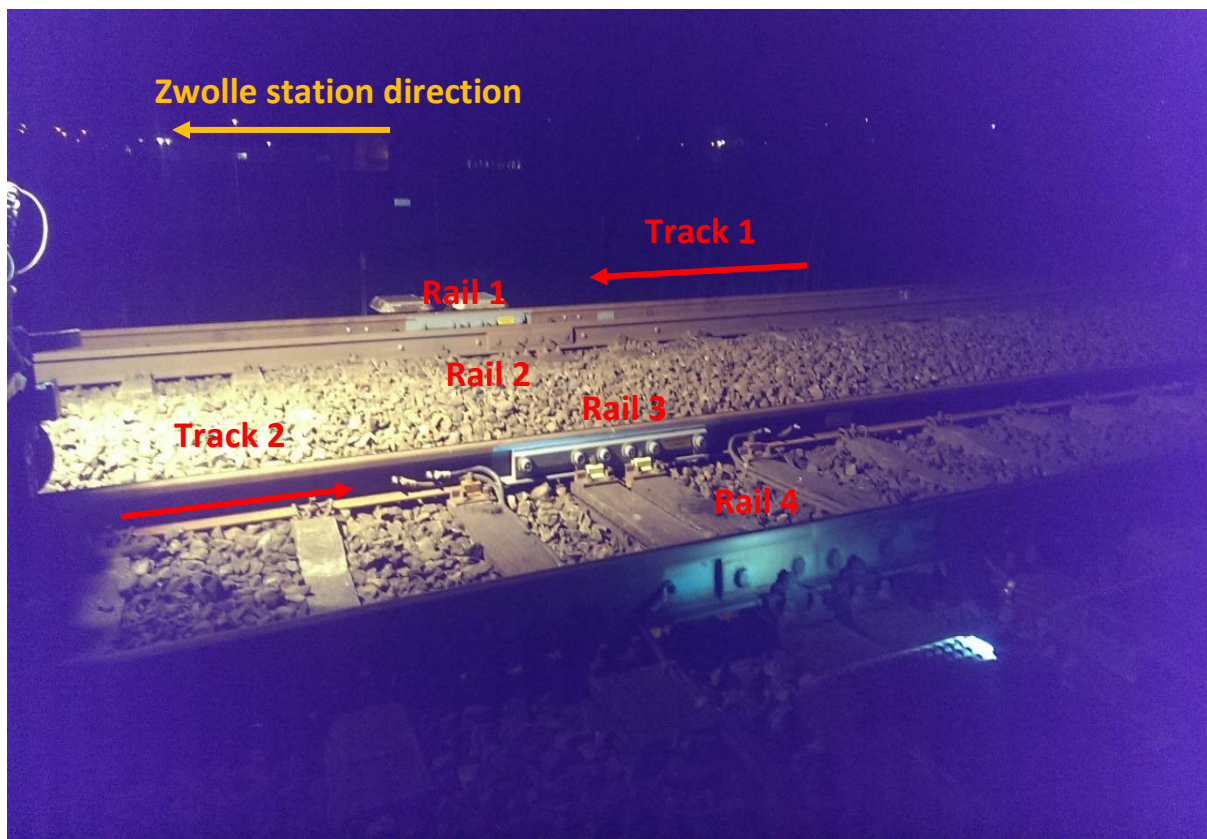


Figure 3.2: Measurements location with the traffic direction of the two tracks

### 3.3 Set-up of the hammer test

The set-up of the hammer test, used to identify the dynamic behaviour of the NRG and the normal joint, can be seen in figure 3.3. The set up consists of the PAK system, uni-directional accelerometers, cables and magnets. Ten uni-directional accelerometers (Brüel & Kjær 4514) were installed in total. Six accelerometers were placed at the top of the rail (fixed with a magnet), two accelerometers in the fishplate and two at the sleepers. The excitation force was measured with a force sensor. Accelerometers 1-3 were placed in characteristic points; namely at the rail end (where impact occurs), above the sleeper (on support) and between two sleepers (mid-span), respectively. Accelerometers 4-6 were placed symmetrically to accelerometers 1-3 with respect to the joint, to identify the transmission of the vibrations on the other side of the joint. Accelerometers 7 and 8 were placed in the middle of the fishplate and between bolts 1 and 2 respectively to identify the transmission of the vibrations of the insulation layer to the fishplate. Accelerometers 9 and 10 were placed at the top of the sleepers to identify the transmission of the vibrations from the rails to the sleepers. In all four rails the accelerometers had the same set-up (with respect to the train direction, accelerometers 1-3 were placed after the end-post while 4-6 before the end-post).

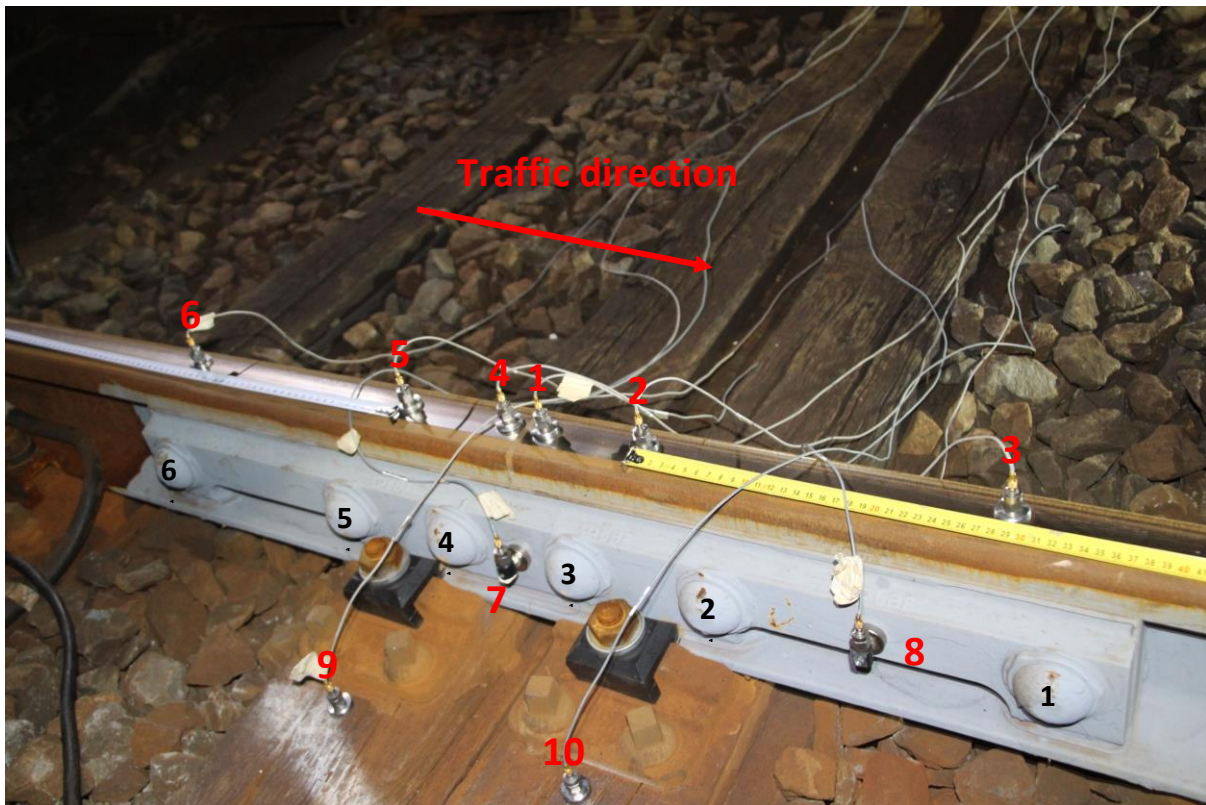


Figure 3.3: Distribution of the accelerometers along the track (red), bolt number (black)

Two instrumented hammers were used. For the high frequencies a hammer with a hard metal tip was used (small hammer). For the low frequencies a hammer with plastic metal tip was used (big hammer). The performed hammer tests using the small and the big hammer can be seen in the figure 3.4a and 3.4b respectively. The excitation point using the small hammer was about 1cm away from the accelerometers 1-6. For the big hammer the excitation point was about 1cm away from the accelerometers 2,3,5,6.

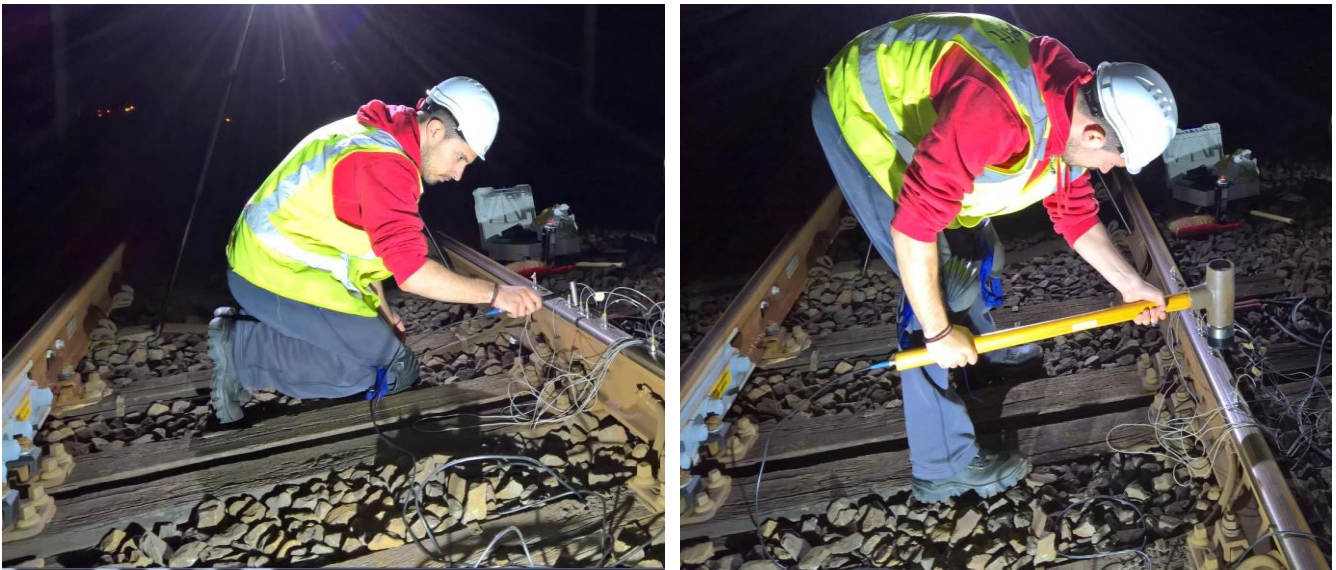


Figure 3.4: a) small hammer b) big hammer

### 3.4 Measurements procedure – post processing

The procedure of the performed hammer tests is as follows: The rail was vertically excited  $F_i(t)$  at six points (points 1-6 according to figure 3.3) for multiple times and the response  $a_i(t)$  was measured for the ten locations of interest.

To increase the reliability of the measurements, the rail was excited 6 times. Then, the average force  $F(t)$  and the average acceleration  $a(t)$  are calculated over the six signals. The input and the output data were recorded using a sampling frequency of 40kHz. A low-pass Butterworth filter with a cut-off frequency ( $f_c$ ) of 5kHz is then applied. The averaged force and acceleration signals are analysed in the frequency domain using a frequency response function (FRF). The FRF is in accelerance format, relating force input and acceleration output according to:

$$H_a(f) = \frac{S_{aF}(f)}{S_{FF}(f)} \quad (3.1)$$

$S_{aF}$  = complex cross-spectrum of acceleration (output) [ $\text{mN/s}^3$ ]

$S_{FF}$  = power spectrum of force (input) [ $\text{N}^2/\text{s}$ ]

The measured accelerance functions show the response of IRJs for vibrations in terms of acceleration over force as a function of vibration frequencies. Plotting the accelerance function against frequency, the resonance and anti-resonance and their characteristic frequencies of the NRG and normal joint can be identified by peaks and dips respectively. In section 4.3 the resonances of the NRG and normal joint are identified and compared with literature.

### 3.5 Distance of the sleepers

Besides the post processing of the obtained measured accelerations, a further observation and analysis of the measurements and track condition can give us valuable information. In figure 3.5 the measured sleeper distances can be seen. It is obvious that the sleeper distances in some points are far from the nominal case (60cm).

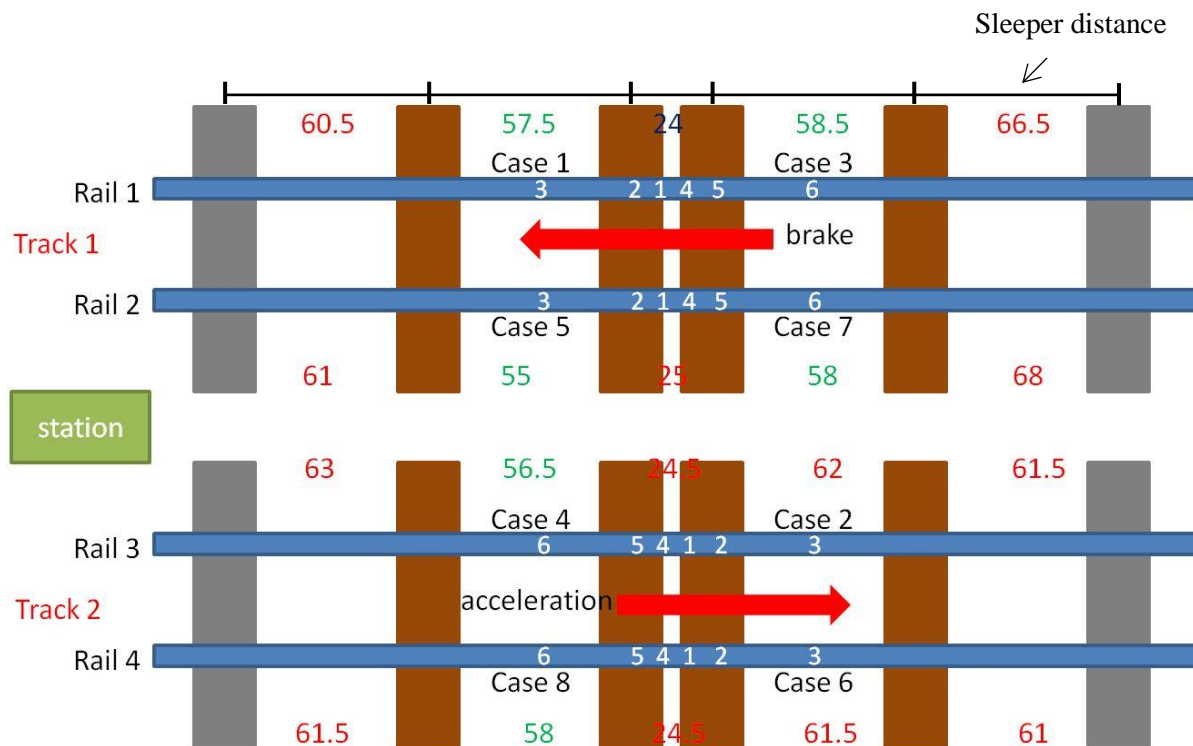


Figure 3.5: Measured sleeper distances (red: larger than 60cm, green: lower than 60cm)

In order to examine the effect of the sleeper distance to the dynamic behaviour of the IRJs, the direct FRFs are plotted in the characteristic points (1-6) for every rail. Positions 1,4, 2,5 and 3,6 are plotted in one graph, because they are located symmetrically with respect to the joint, so they should have comparable responses.

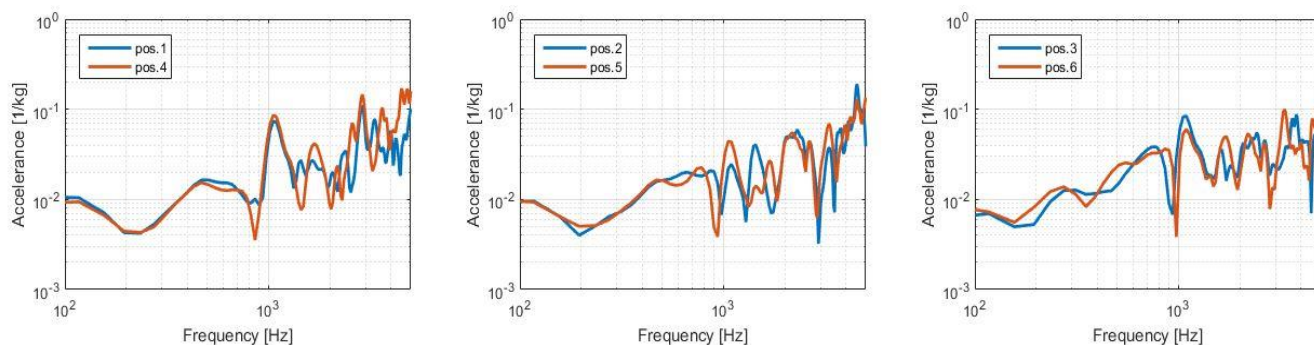


Figure 3.6: Direct FRF for rail 1. a) position 1,4 b) position 2,5 c) position 3,6

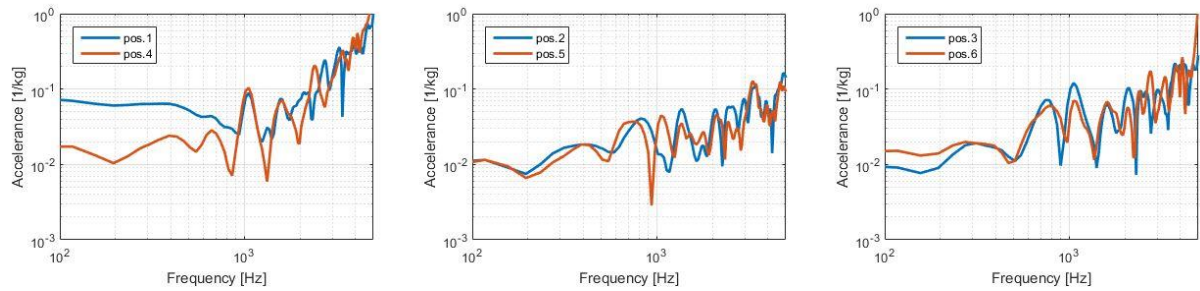


Figure 3.7: Direct FRF for rail 2. a) position 1,4 b) position 2,5 c) position 3,6

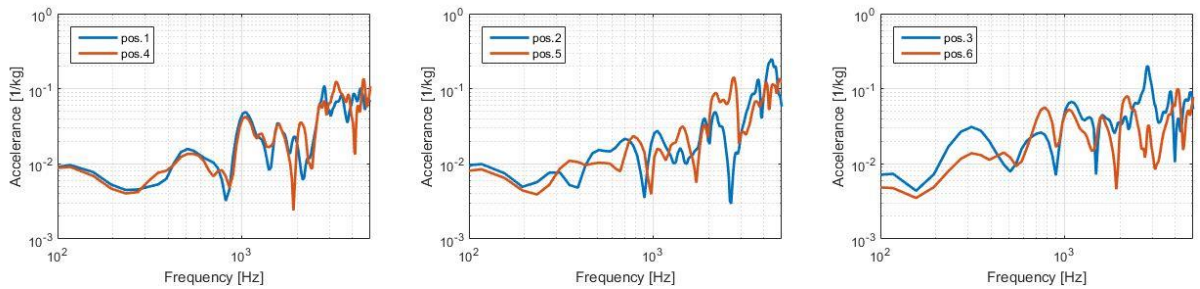


Figure 3.8: Direct FRF for rail 3. a) position 1,4 b) position 2,5 c) position 3,6

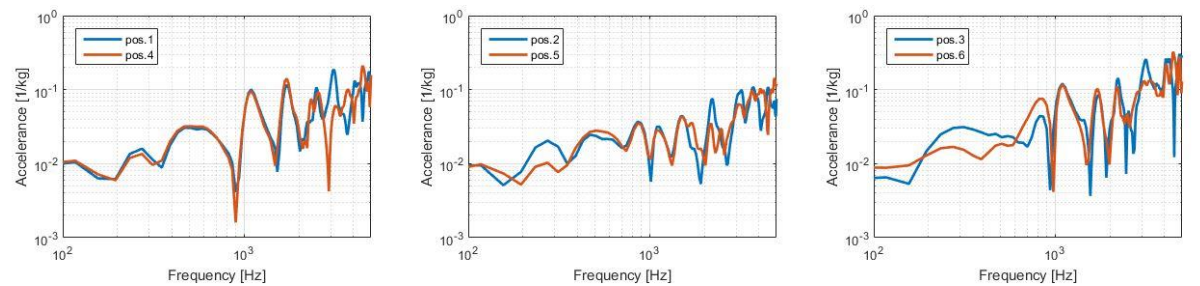


Figure 3.9: Direct FRF for rail 4. a) position 1,4 b) position 2,5 c) position 3,6

Two notable findings, regarding the correlation between the sleeper span and the dynamic response of the system, can be obtained by analysing the results:

First, from figures 3.6c, 3.7c and 3.8c it can be deduced that the pinned-pinned resonance in position 6 is lower comparing to position 3; in combination with the sleepers distribution shown in figure 3.5, a pattern can be identified: When the sleepers are less equally distributed, the pinned-pinned resonance has a lower amplitude, and in fact the more the sleeper span is far from nominal, the lower the amplitude for the pinned-pinned resonance is.

Second, when the span between the two wooden sleepers after the joint increases, the rail resonance is higher. This can be clearly seen in figures 3.8c , 3.9c and 3.5 where the rail resonance  $f_r$  in position 3 (sleeper distance 62cm for rail 3 and 61.5cm for rail 4) is higher comparing to position 6 (sleeper distance 56.5cm for rail 3 and 58cm for rail 4).

These two findings will be further investigated by making use of the finite element model in the next chapters.

### 3.6 Comparison of the behaviour of the NRG-joint and the normal-joint

Finally, in this chapter the measured dynamic behaviour of the NRG-joint and the normal joint are compared.

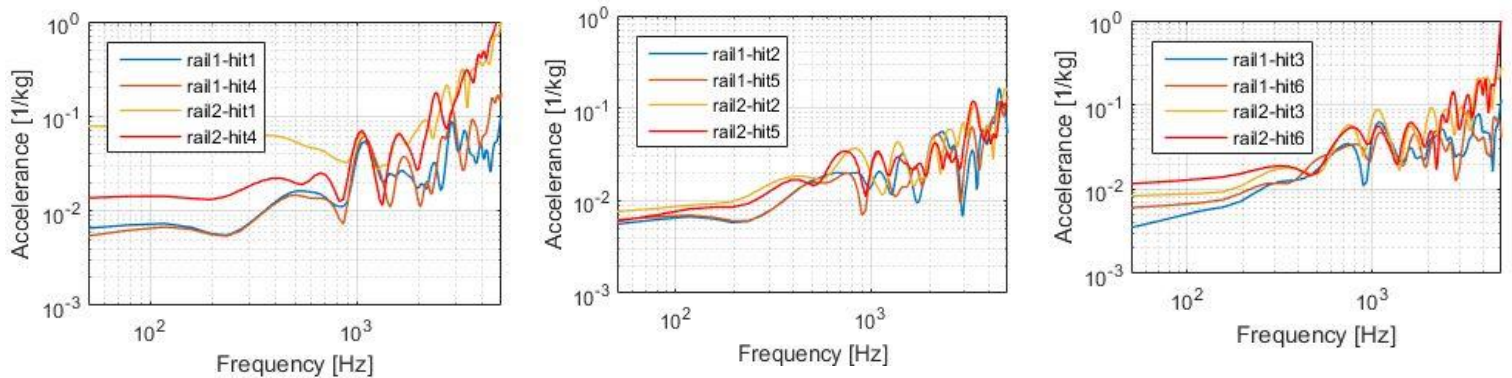


Figure 3.10: Comparison of FRFs for NRG and normal joint - track 1. a) hit1,4 b) hit2,5 c) hit3,6

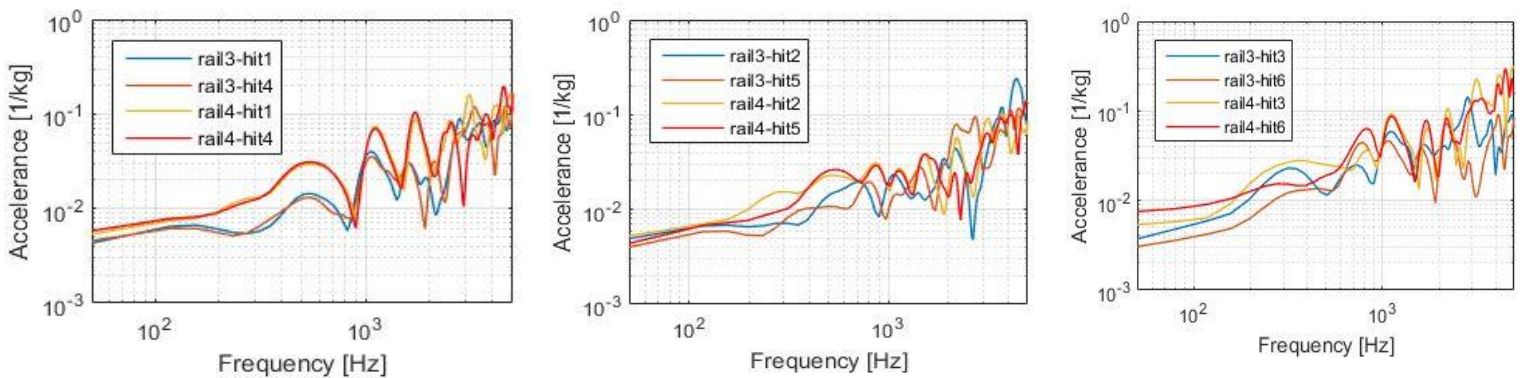


Figure 3.11: Comparison of FRFs for NRG and normal joint - track 2. a) hit1,4 b) hit2,5 c) hit3,6

For track 1 the full track resonance and the rail resonance are higher for the normal joint, while the pinned-pinned resonance is nearly the same for both joints. For track 2 (figure 3.11) the difference in the response between the two joints is more apparent. The full track resonance, the rail resonance, and the pinned-pinned resonance are higher for the normal joint. Although the structure of the two joints is different (different length, mass and shape), the resonant frequencies are the same for both joints installed on track.

## 4. Finite element model

*In this chapter a 3D FE model is established using the nominal geometry of the track components, to reproduce hammer test measurements and to explore the dynamic behaviour of the track. In this study only half-track was considered, to reduce the computational time. This chapter first analyses the sketching of the cross profiles of the rails, insulation layer and the fishplate. The second step is to build the model by using the appropriate elements, material types and boundary conditions. In addition, the computational strategy (implicit to explicit) is further explained. The stiffness and the damping of the rail-pads and the ballast are derived by fitting the results of the FE analysis to the field measurements (calibration). The transfer accelerances of the two models are validated with measurements.*

### 4.1 3D FE model

#### 4.1.1 Geometry modelling

The geometries of the rail, the insulation layer and the fishplate should be modelled as accurately as possible because they play a significant role in the dynamic behaviour of the system. Due to the complex geometries of these parts, their detailed nominal geometries are first designed in AutoCAD and then imported as an IGES extension file in a FEM software (ANSYS). The cross-section of the rail, the insulation layer, and the fishplates can be seen in figure 4.1. The whole assembly is imported in ANSYS with 1/40 inclination (rail inclination).

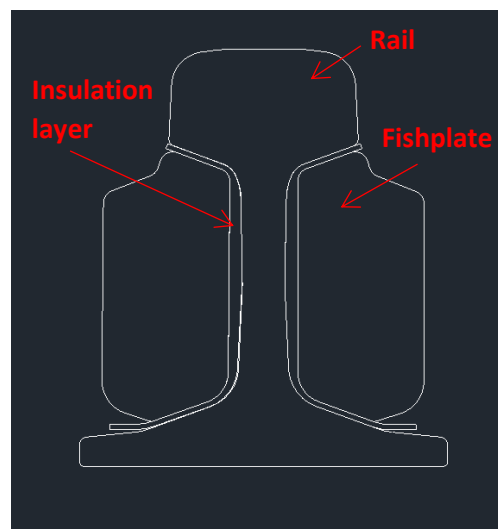


Figure 4.1: Sketching of rail, insulation layer and fishplate

### 4.1.2 Element type – material model

There are different element types and material models available in the FE software. The right choice of the element type and material model is of great importance for a successful FE model. In this section the element type and the material model used in every part of the track are described. Detailed explanation and characteristics of the elements are presented in Appendix A.

#### **Rail**

The rail is modelled using solid elements (SOLID185, SOLID164) with the nominal cross-section geometry of UIC54. The rail is made of steel, so it is modelled as an isotropic material.

#### **Sleeper**

The sleepers are modelled using solid elements (SOLID185, SOLID164) with the nominal geometry of sleeper type NS90. Although the sleepers are made of reinforced concrete, a non-prestressed isotropic elastic material is considered. Wooden sleepers are used beneath the IRJ, and concrete sleepers elsewhere. Despite the fact that wood is an orthotropic material[44-46], it was assumed as isotropic. The sleepers are considered under nominal conditions and they connected with the ballast elements at some points.

#### **Rail-pad**

The geometry of the rail-pad is neglected for the sake of simplicity. In reality, the fastening system consists of the rail-pads and the clamps which fix the rail to the support, but the fastening models simplified as pairs of springs and dampers has been proved to be reliable for calculating dynamics within frequency range between 50Hz and 1400Hz. The rail-pad is represented using 27 pairs of one linear spring and viscous damper element (COMBIN14, COMBI165) with stiffness and damping properties  $K_r$  and  $C_r$  respectively. Three rows of nine spring-damper pairs are distributed in each sleeper. Different values of stiffness ( $K_{rc}$ ,  $K_{rw}$ ) and damping ( $C_{rc}$ ,  $C_{rw}$ ) were used for the rail-pads of concrete and wooden sleepers respectively.

#### **Ballast**

Similarly to the rail-pads, the geometry of the ballast is neglected. The ballast is represented using 15 pairs of one linear spring and viscous damper element (COMBIN14, COMBI165) with stiffness and damping properties  $K_b$  and  $C_b$ , respectively.

## Fishplate

The fishplate is modelled using solid elements (SOLID185, SOLID164) with its nominal cross-section geometry. The fishplate is also made of steel, so it is modelled as an isotropic material.

## End post layer

Results from previous studies [47] conclude that only a small amount of the applied force is carried by the end post layer. Consequently, this layer is numerically modelled as a gap in the current study. This simplification should have insignificant effect on the results since the elastic modulus of this layer is much lower than that of the rail ( $1.5 \cdot 10^9$  N/m<sup>2</sup> and  $2.1 \cdot 10^{11}$  N/m<sup>2</sup>, respectively).

## Insulation layer

According to literature, the insulation layer is a composite material consisting of many layers (approximately 10) of glass fibres and epoxy.

For the insulation layer three material models are proposed, namely:

- i) isotropic
- ii) specially orthotropic (or transverse isotropic)
- iii) specially orthotropic with many layers

Among the three models, the second model is chosen for the analysis in this study. The reason is that the first model is not realistic (since it is a composite material, which does not have the comparable properties in every direction), and the third model is too complex and inefficient for modelling.

The insulation layer is modelled using solid elements (SOLID185, SOLID164) with its nominal cross-section geometry. The calculation of the mechanical properties of the insulation layer is presented in section 4.1.6.

### 4.1.3 Constrains

The bottom ballast nodes of the ballast elements are fixed in all three directions (x, y, z), while the upper nodes, which are connected to the sleepers, are fixed in the longitudinal (z) and lateral (x) directions. The upper nodes of the rail-pad elements are connected to the rail, and the bottom rail-pad nodes, connected to the sleepers, are fixed in the longitudinal (z) and lateral (x) directions. The upper nodes of the sleeper elements, which are connected to the rail-pads, are coupled with the corresponding bottom nodes of the sleeper elements in the vertical (y) direction.

### 4.1.4 Load

For the implicit analysis (see section 4.2) only the loads of bolt pretension and gravity are applied to the IRJ model.

In the explicit analysis (see section 4.2) a hammer test is reproduced. The hammer force is simulated as a force applied at the top of the rail. The force has triangular shape in the time domain with zero magnitude before  $t_0$ , maximum magnitude ( $F_{\max}$ ) at  $t_1$  and zero magnitude after  $t_2$ , as shown in figure 4.2.

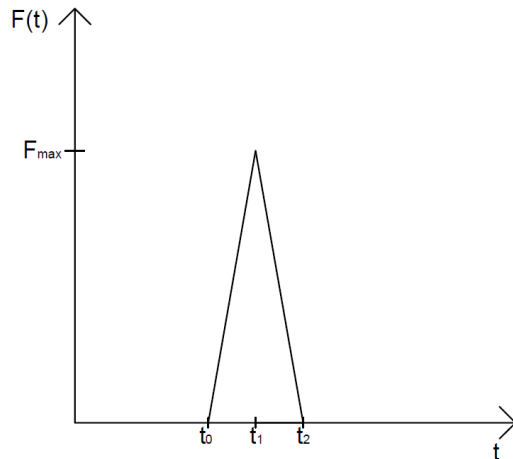


Figure 4.2: Hammer force

#### 4.1.5 Mesh

In the current IRJ model, the rail is meshed homogeneously using 10mm elements. In this way the model can give accurate results (it has been benchmarked with simulations, with smaller element size of 1mm, which gives quite similar results) and at the same time it is computationally efficient. The fishplates and the insulation layer are also meshed using 10mm element size. The sleepers are meshed using coarser mesh except in the region of the rail-pads connection.

#### 4.1.6 Mechanical properties of the track components

The density and elasticity properties ( $\rho$ ,  $E$ ,  $\nu$ ) required for the simulation of each material are presented in table 4.1

component	material	Young's Modulus $E$	Poisson's ratio $\nu$	Density $\rho$	Yield stress	Tangent Modulus
rail, fishplate	steel	210 GPa	0.3	7800 kg/m <sup>3</sup>	500 MPa	21 GPa
NS90 sleeper	concrete	38.4 GPa	0.2	2520 kg/m <sup>3</sup>	-	-
wooden sleeper	wood	20 GPa	0.3	1300 kg/m <sup>3</sup>	-	-

Table 4.1: Mechanical properties of track components

Fiberglass epoxy can be characterised as a composite transverse isotropic material [16] with three mutually perpendicular planes of symmetry. Those planes are defined in the longitudinal direction (L) along the fibres, the radial direction (R) and the tangential direction (T). To fully characterise the mechanical behaviour of fiberglass epoxy it is necessary to know the stress-strain relationship referred to the LRT reference frame. The only way to obtain these data accurately is by performing mechanical tests, however, due to confidentiality reasons, testing of the material is not available. Hence, the mechanical properties of the insulation layer are calculated according to the “rule of mixtures” [16] for unidirectional fibres. The following formulas are used:

$$E_{11} = V_f \cdot E_f + V_m \cdot E_m \quad (4.1)$$

$$E_{22} = E_{33} = \frac{E_f \cdot E_m}{V_f \cdot E_m + V_m \cdot E_f (1 - \nu_m^2)} \quad (4.2)$$

$$\nu_{12} = \nu_{13} = V_f \cdot \nu_f + V_m \cdot \nu_m \quad (4.3)$$

$$G_{12} = G_{13} = \frac{G_f \cdot G_m}{G_m \cdot V_f + G_f \cdot V_m} \quad (4.4)$$

$$\nu_{23} = \nu_{12} \frac{1 - \nu_{21}}{1 - \nu_{12}} \quad (4.5)$$

$$G_{23} = \frac{E_{22}}{2(1 + \nu_{23})} \quad (4.6)$$

$$\rho_c = \rho_f \cdot V_f + \rho_m \cdot V_m \quad (4.7)$$

Nominal values according to literature are used for the glass fibres and for the epoxy [16],[48-52]. The nominal and the calculated values can be seen in table 4.2, 4.3 and 4.4. The insulation layer thickness is 2mm. The percentage of epoxy ( $V_m$ ) was taken equal to 45%.

	<b>Parameters</b>	<b>Nominal values</b>
<b>Fiberglass</b>	Young's Modulus $E_f$ (GPa)	72
	Poisson's ratio	0.22
	Density $\rho_f$ (kg/m <sup>3</sup> )	2550

Table 4.2: Mechanical properties of fiberglass

<b>Epoxy</b>	<b>Parameters</b>	<b>Nominal values</b>
	Young's Modulus $E_m$ (GPa)	4
	Poisson's ratio	0.35
	Density $\rho_m$ (kg/m <sup>3</sup> )	1200

Table 4.3: Mechanical properties of epoxy

<b>Parameters</b>		<b>Calculated values</b>
<b>Fiberglass epoxy insulation layer</b>	$E_{11}$ (modulus of elasticity in the fiber direction)	41.4 GPa
	$E_{22}$ (modulus of elasticity in the direction transverse to the fibers)	8.23 GPa
	$E_{33}$ (modulus of elasticity in the direction transverse to the fibers)	8.23 GPa
	Shear modulus $G_{12}$ (in-plane shear modulus)	3.1 GPa
	Shear modulus $G_{13}$ (in-plane shear modulus)	3.1 GPa
	Shear modulus $G_{23}$ (out of plane shear modulus)	3.05 GPa
	Poisson's ratio $\nu_{12}$	0.2785
	Poisson's ratio $\nu_{13}$	0.2785
	Poisson's ratio $\nu_{23}$	0.365

Table 4.4: Mechanical properties of uni-directional fiberglass-epoxy

#### 4.1.7 Contact

Two contact pairs are defined, one between the insulation layers and the rail, and the other between the insulation layers and the fishplate. CONTA174 and TARGE170 elements (see

Appendix A) are used to define the contact for these pairs. The friction coefficient is defined as 0.3. The Augmented Lagrange method (see Appendix B) is implemented as contact algorithm.

## 4.2 ANSYS – LS DYNA simulation process

### ANSYS implicit analysis

In order to capture the hammer-excited track vibration, first an initialisation step is performed with implicit analysis. This quasi-static analysis calculates rail response under gravity and the action of bolts pretension. In this nonlinear implicit analysis, solution of each step requires a series of trial solutions (iterations) to establish equilibrium within a certain tolerance. The calculation of current quantities in one time step is based on the quantities calculated in the previous time step. Implicit analysis requires a numerical solver to invert the stiffness matrix once or even several times over the course of a load/time step. This matrix inversion is an expensive operation, especially for large models. Large initial gap or too much initial penetration between the contact bodies should be avoided. If such situations occur, the implicit solution may not converge because the contact pairs (rail-insulation layer, insulation layer-fishplate) are out of contact. The current model has an increased number of frictional contacts, inserting non-linearities to the model which make the solution more difficult to converge.

For the presented model, the computational time of the implicit analysis is about 1 hour.

### LS DYNA explicit analysis

At the end of the implicit analysis, the nodal displacements and stresses are written in a text result file. At the beginning of the explicit analysis, this text file is invoked, and the nodal displacements and stresses resulted from the implicit analysis are used as initial conditions for the explicit analysis.

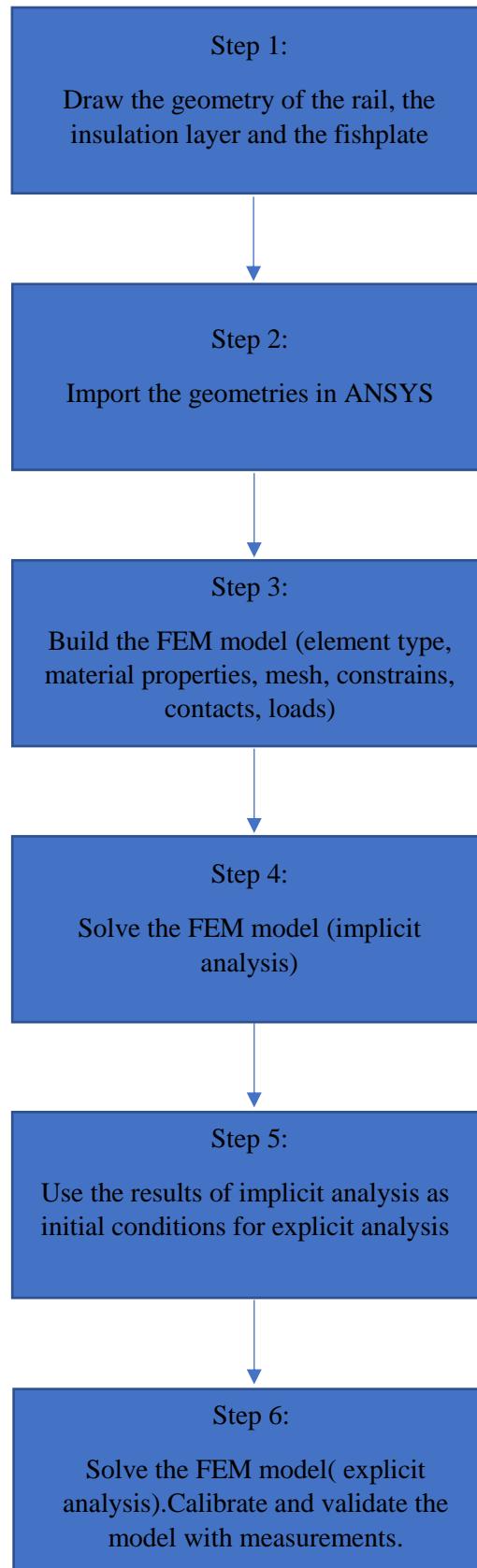
For the explicit analysis the computational time depends on the time step. The time step in explicit analysis must be less than the Courant time step (time it takes a sound wave to travel across an element). The critical time step is defined as follows:

$$\Delta t_{\min} = \frac{l}{c} \quad \text{where } l = \text{length of the element and } c = \text{wave propagation velocity, defined as}$$

$$\text{follows: } c = \sqrt{\frac{E}{\rho}} \quad \text{where } E = \text{Young's modulus and } \rho = \text{density}$$

ANSYS LS-DYNA applies a scale factor of 0.9 (default) to the critical time-step for stability reasons. For the presented model the critical time step is  $\Delta t = 2,33 \cdot 10^{-7}$  seconds and the simulation time 0,05 seconds. The computational time is approximately 6-7 hours.

A summary of the computational strategy is illustrated in the flow chart below:



In the figures below the FE models of the two types of joint can be seen:

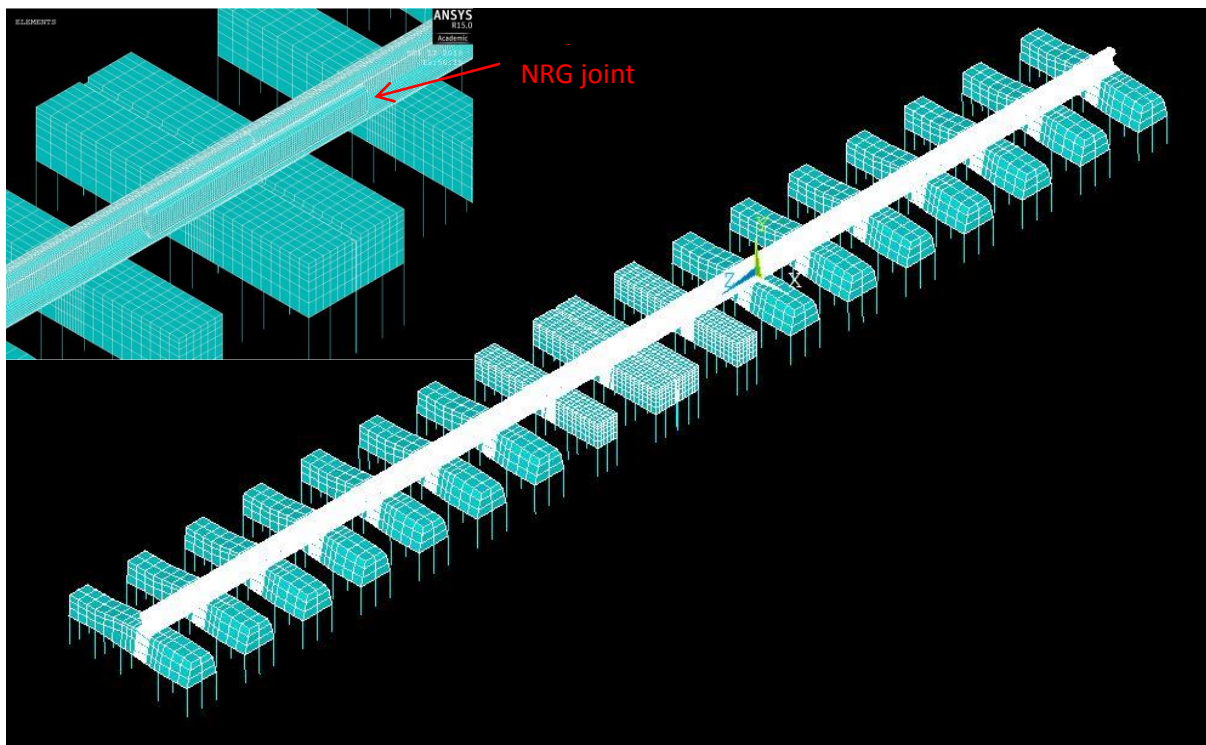


Figure 4.3: FE model of the NRG joint

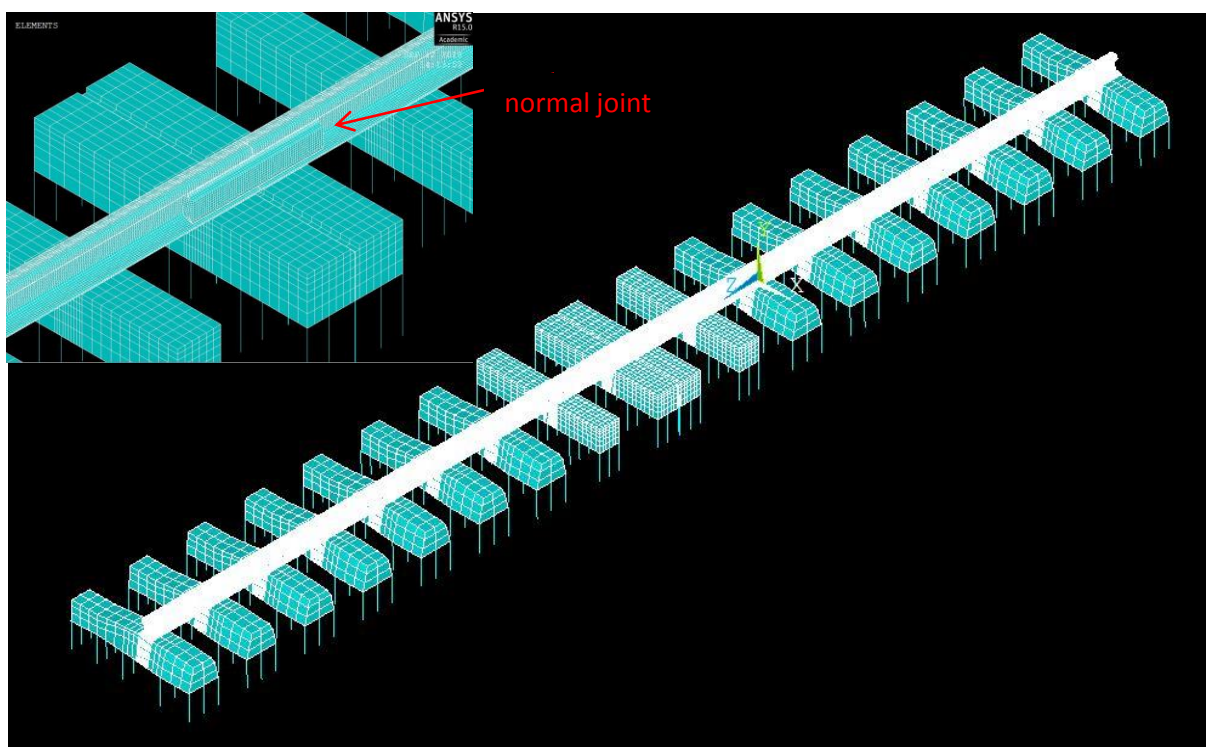


Figure 4.4: FE model of the normal joint

### 4.3 Calibration of the numerical model/ Deriving track parameters

In order to fit the results of the numerical analysis to the field measurements a parametric analysis is performed using as variables the stiffness and damping of the rail-pads and the ballast. In this section, the measured direct accelerances (response and excitation are measured in the same location and direction) are used to calibrate the stiffness and damping parameters involved in the FE model by fitting their levels and resonant frequencies to the simulation results. The resulting values of the stiffness and the damping for the rail-pads of concrete and wooden sleepers and for ballast for both joints can be seen in the table below:

Parameters		Calibrated values	
NRG	Rail-pads of concrete sleepers	Stiffness $K_{rc}$	1500 MN/m
		Damping $C_{rc}$	65000 Ns/m
	Rail-pads of wooden sleepers	Stiffness $K_{rw}$	15 MN/m
		Damping $C_{rw}$	65000 Ns/m
	Ballast	Stiffness $K_b$	45 MN/m
		Damping $C_b$	40000 Ns/m
normal	Rail-pads of concrete sleepers	Stiffness $K_{rc}$	2000 MN/m
		Damping $C_{rc}$	62000 Ns/m
	Rail-pads of wooden sleepers	Stiffness $K_{rw}$	58 MN/m
		Damping $C_{rw}$	60000 Ns/m
	Ballast	Stiffness $K_b$	45 MN/m
		Damping $C_b$	40000 Ns/m

Table 4.5: Calibrated values for the two joints

The following notation is used for the graphs of this chapter: rail 1,3 (NRG joint is installed), rail 2,4 (normal joint is installed). Hit1-6 are the hits in points 1-6 according to figure 4.3. Hit1-hit4, hit2-hit5 and hit3-hit6 are plotted in the same graph because points 1,4 2,5 and 3,6 are symmetric with respect to the joint. (see also figures 3.2 and 3.3)

The closest fits between the numerical and measured direct accelerances for the NRG and normal joint are shown in figures 4.5 and 4.6 respectively.

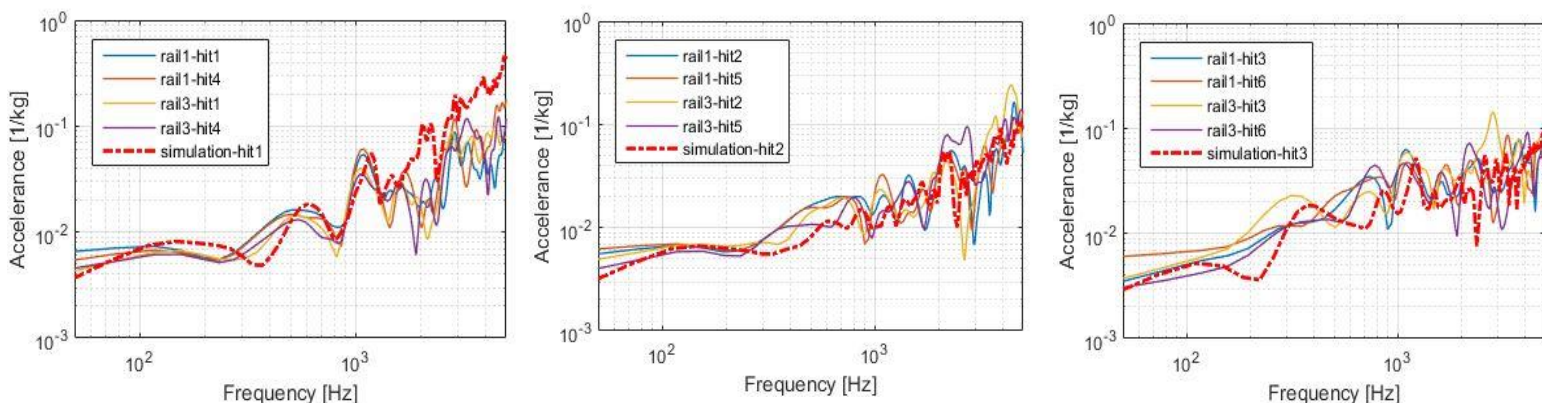


Figure 4.5: Direct FRF for the NRG-joint. a) hit1,4 b) hit 2,5 c) hit 3,6

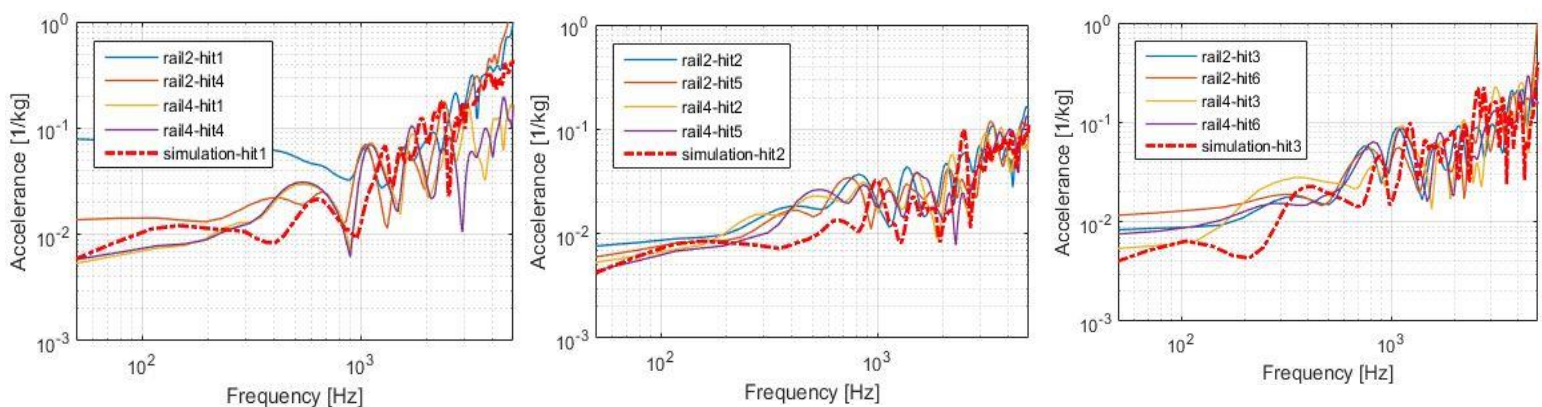


Figure 4.6: Direct FRF for the normal joint. a) hit1,4 b) hit 2,5 c) hit 3,6

The numerical models for both joints show good agreement with the field measurements up to the frequency of 1400 Hz. The vibration modes that have been presented in section 2.2 can be clearly identified from the model and the measurements. A peak can be observed in the frequency region of 100Hz which corresponds to the full track resonance ( $f_i$ ), for both the measurements and the FE model. Measured sleeper anti-resonance ( $f_s$ ) occurs at 234Hz, while for the model occurs at 330Hz. A clear peak can be observed at about 510Hz (measured value), which represents the rail resonance ( $f_r$ ). For the model this peak is observed at 595 Hz. The pinned-pinned resonance occurs between 1055Hz and 1094Hz for both joints, according to the measurements, while this value is 1188Hz for the numerical model. The deviations in the pinned-pinned resonance between the measurements and the model can be caused due to sleeper distribution of the measured tracks, which is not nominal (see section 3.4). After the frequency of 1400 Hz large deviations exist between the model and the measurements, as well as the measurements themselves.

## 4.4 Effect of the system parameters

In order to understand how each parameter affects the behaviour of the IRJ, a parametric study is conducted, changing every time only one of the parameters (rail-pad stiffness, rail-pad damping, ballast stiffness, ballast damping). For the reference case the calibrated values of the NRG-joint, that are presented in table 4.5 are used. Every parameter is changed every time by a factor two.

### Effect of ballast

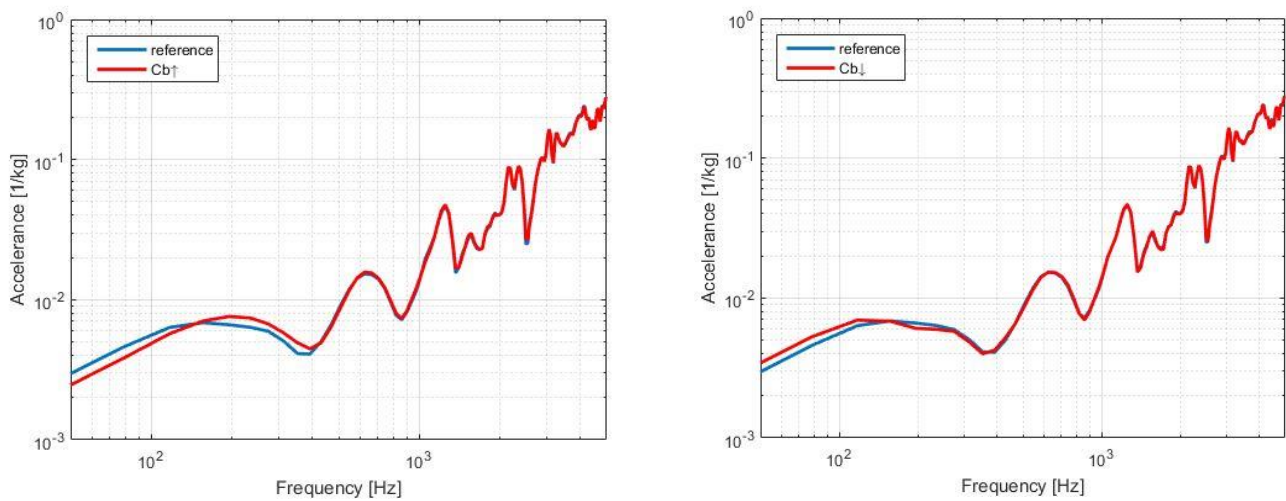


Figure 4.7: Accelerance function with varying vertical damping for ballast

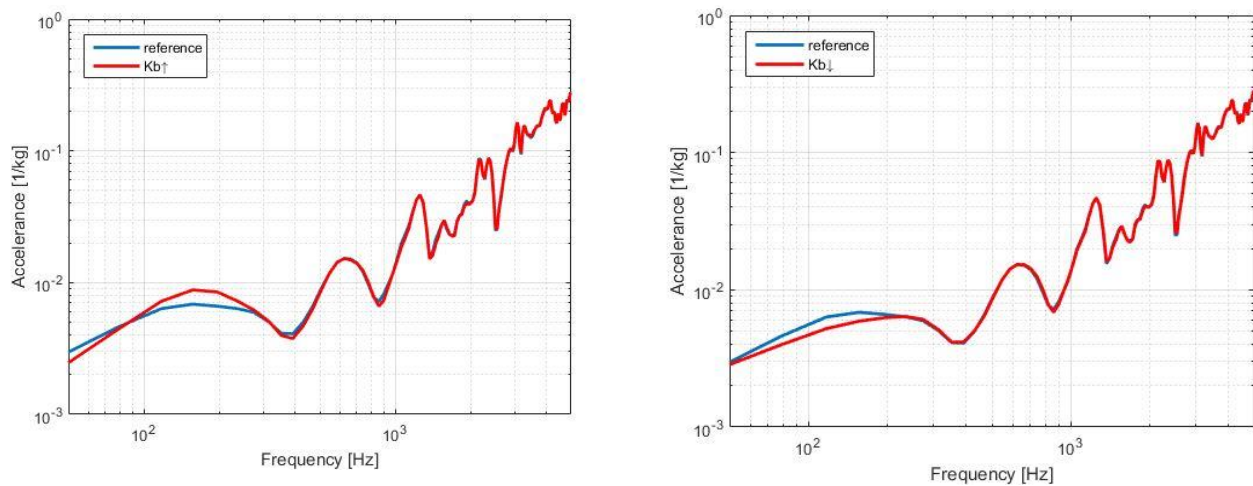


Figure 4.8: Accelerance function with varying vertical stiffness for ballast

Ballast damping mainly affects the track dynamic properties below 400Hz as it can be seen from figure 4.7. An increase in the ballast damping leads to lower acceleration amplitude in the frequency range of 50Hz and 150 Hz; on the contrary has the opposite effect in the frequencies between 150Hz and 300Hz. Figure 4.8 shows that the change of ballast stiffness has an effect in the region between 50Hz and 300Hz. Increase of ballast stiffness leads to the increase of amplitude of the full track resonance.

### **Effect of the rail-pads**

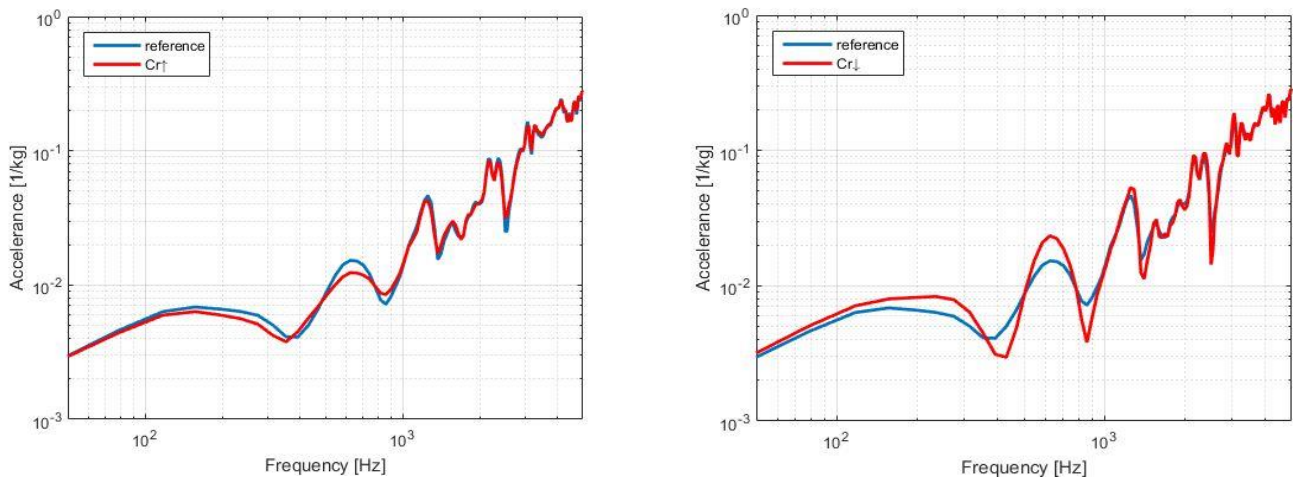


Figure 4.9: Accelerance function with varying vertical damping for rail-pads

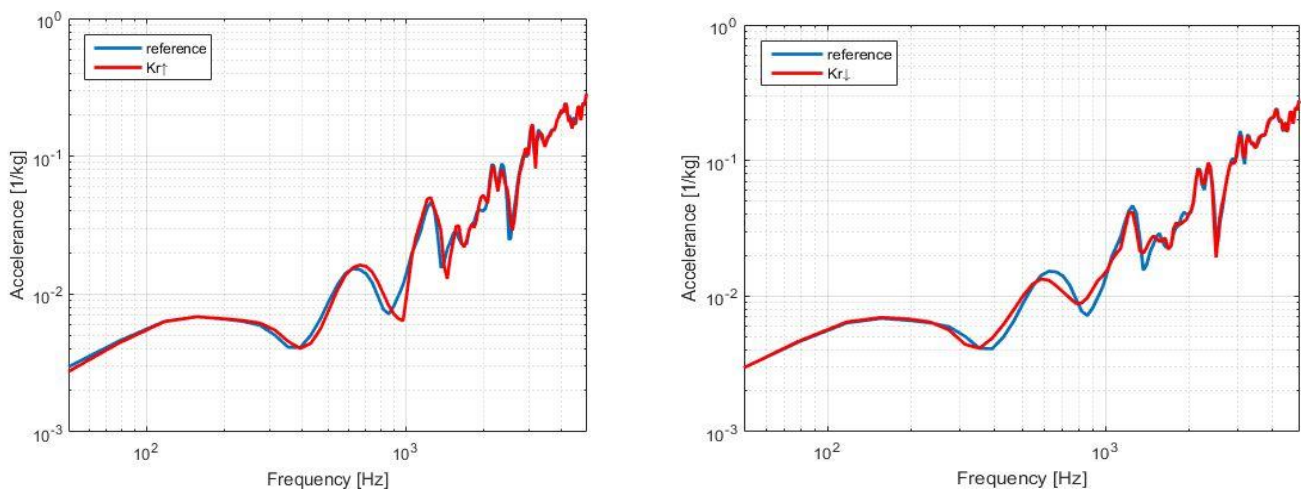


Figure 4.10: Accelerance function with varying vertical stiffness for rail-pads

From figure 4.9 it is obvious that a change in the rail-pads damping has effects on the amplitude of the accelerance function in the region between 100Hz and 1000Hz, but no effect on the resonance frequencies. Decreasing the damping of the rail-pads leads to higher amplitudes and sharper dips and peaks.

From figure 4.10 it can be seen that the change of the rail-pads stiffness has an effect in the region between 300Hz and 1300Hz. Decreasing rail-pad stiffness causes a shift to the resonance frequencies leftwards. At the same time, the amplitude of the accelerance function decreases, while the peaks and the dips become less sharp.

The change of stiffness and damping of the rail-pads has no noticeable influence in the pinned-pinned resonance.

## 4.5 Validation of the transfer accelerances

The stiffness and damping values (of rail-pads and ballast) calibrated by the direct accelerances, are used in the simulations of the transfer accelerances to validate the dynamic behaviour of the FE model. In order to validate the model, the rail is excited at position 1 (see figure 3.3) and the vibration responses of positions 1-8 (see figure 3.3) are examined. The results of the models are compared with the measurements results in figures 4.11 and 4.12.

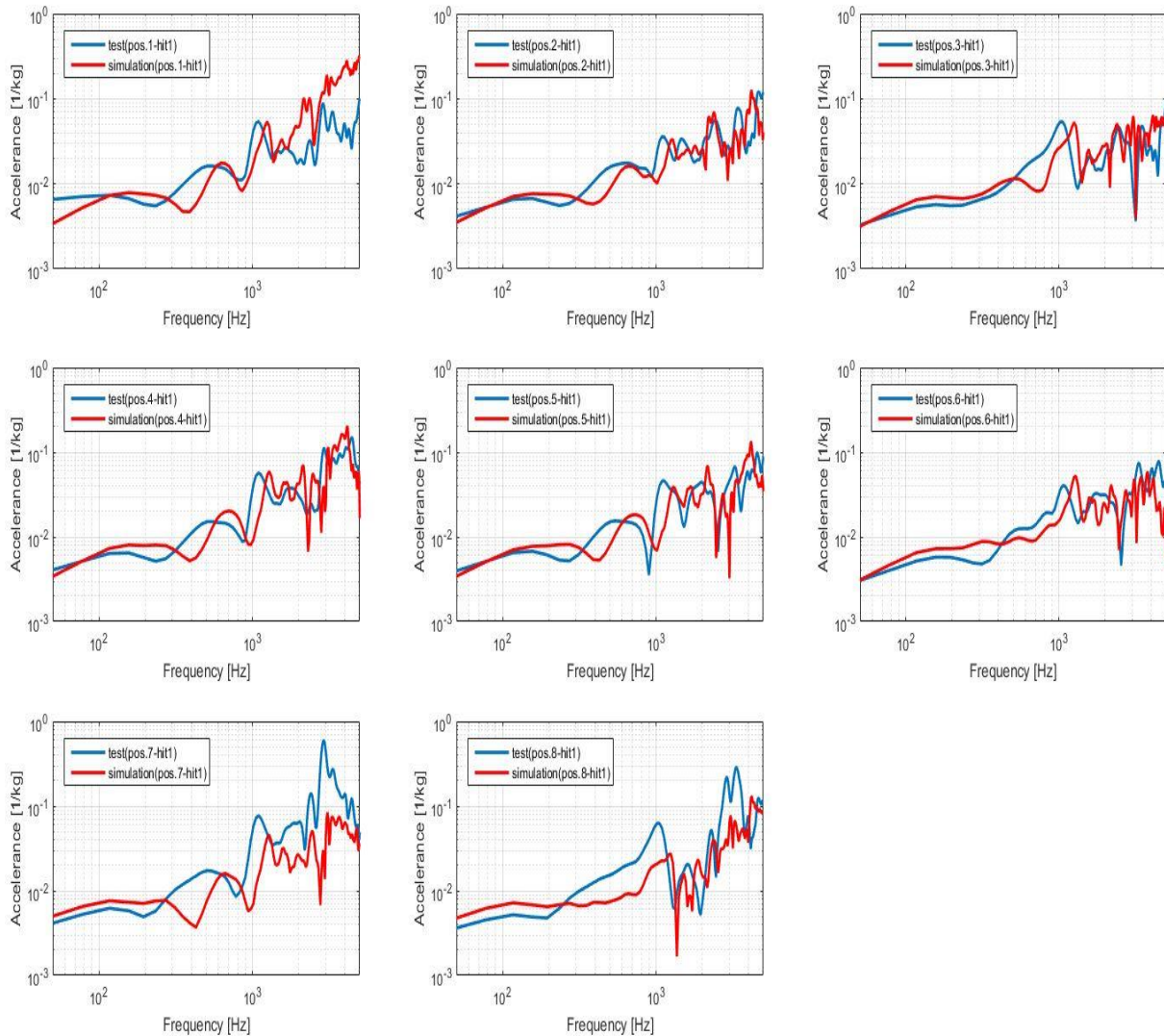


Figure 4.11: Validation of transfer accelerances for the NRG-joint

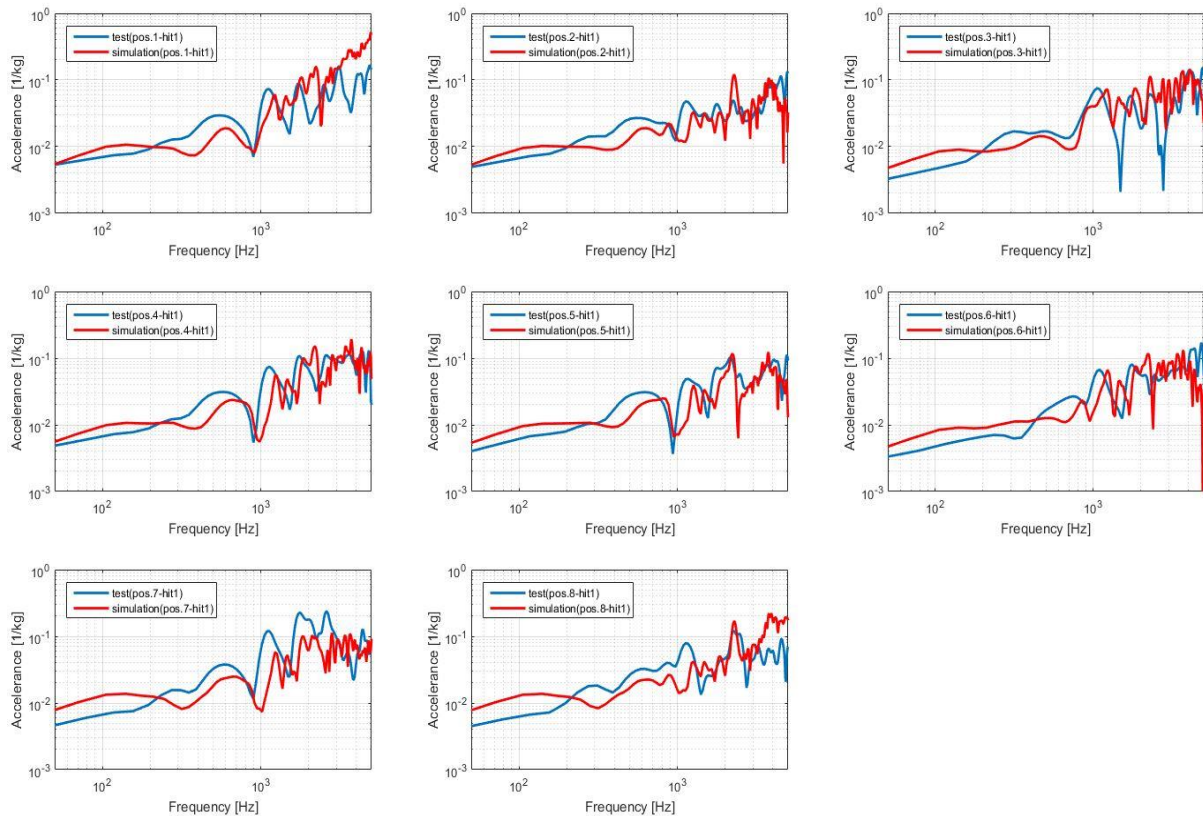


Figure 4.12: Validation of transfer accelerances for the normal joint

From figures 4.11 and 4.12 it can be deduced that the two numerical models follow the trend of the measurements up to the frequency of 1400Hz. The full track resonance occurs at the same frequency for the measurements and the two models (approximately 100Hz). The rail resonance ( $f_r$ ) frequency, the sleeper anti-resonance ( $f_s$ ) frequency and the pinned-pinned resonance ( $f_{pp}$ ) frequency are offset to the right for the numerical models, compared to the measurement. This can be due to the different sleeper span used in the simulation and measurements, as described in section 3.4. The amplitude of resonances for the numerical models and the measurements has the same level.

## 4.6 Concluding remarks

The presented FE models are calibrated and validated with the measurement results. As it can be seen from figures 4.11 and 4.12 the models are capable to accurately identify the dynamic behaviour of the two joints up to the frequency of 1400Hz (the types of resonance presented in section 2.2 can be reproduced from the FE models). Ballast properties affect the dynamic behaviour of the joints in the middle frequency range (50-300Hz), while rail-pad properties affect the dynamic behaviour of the joints in the middle and high frequency range (300-1100Hz). A shift to the right is observed for the resonance frequencies of the model comparing to the measurements results and this can be caused due to the sleeper span (not nominal at some points) and due the condition of the track (e.g. damages that cannot be seen by naked eye).

## 5. Performance optimisation

*The dynamic behaviour of the IRJ has been analysed and the numerical model has been validated, in the previous chapters. An optimisation strategy is proposed in this chapter. Optimisation of a mechanical system generally means improving the system performance during the working cycles under some manufacturing, operational and failure conditions as well as cost limitations. Combining measurement results and observations, validated FE models are developed with different sleeper span distributions, aiming to reduce certain resonances of IRJ.*

### 5.1 Pinned-pinned resonance

As it was mentioned in section 2.2.2, pinned-pinned resonance is one of the characteristic vibration modes of rails and beams, that are discretely supported with uniform span. It first occurs when the wavelength  $\lambda$  of the rail bending waves is twice the support span (figure 5.1). It appears also in higher modes, but the 1<sup>st</sup> mode has the highest amplitude. This vibration is poorly damped; since, the vibrating displacement is located in the rail, and its associated damping is mainly due to its own internal damping. The response to an excitation at this frequency strongly depends on exciting position. It is maximum at the mid of a span, and minimum above the sleeper, leading to a resonance and an anti-resonance, respectively. Among other track resonances, pinned-pinned resonance plays an important role in noise and vibration radiation of the rails and can be used as a meaningful instrument in track system dynamics recognition and optimisation [53].

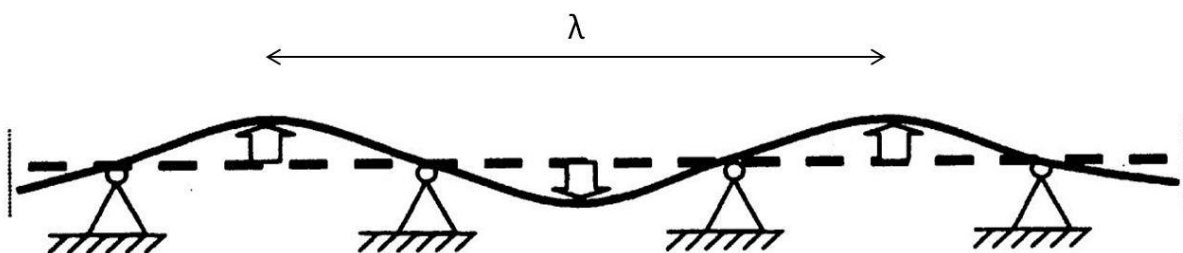


Figure 5.1: 1<sup>st</sup> order pinned-pinned resonance

## 5.2 Optimisation of sleepers distribution

Both the measurement results and the numerical model are capable of reproducing the vibration modes presented in section 2.2. Within the framework of this thesis, the pinned-pinned resonance is chosen for further investigation. Using the findings from the measurements (illustrated in section 3.5), optimisation strategies of sleeper distribution are proposed to reduce the pinned-pinned resonance  $f_{pp}$  and rail resonance  $f_r$ . The validated FE IRJ models are employed to show the effects of the optimisation strategies.

The theoretical background for the optimised sleeper distribution is that the 1<sup>st</sup> order pinned-pinned resonance occurs when the wavelength is exactly twice the support span, so by changing the uniform sleeper distribution this type of resonance can be reduced. To examine the difference in the simulated responses, the sleeper distance on one side of the joint remains the same, while on the other side, the first two sleeper spans are modified (figure 5.2). Three different cases are examined, at which the spans  $a$  and  $b$  (figure 5.2) were given different values. Then the two direct FRFs of position 3 and 6 are compared.

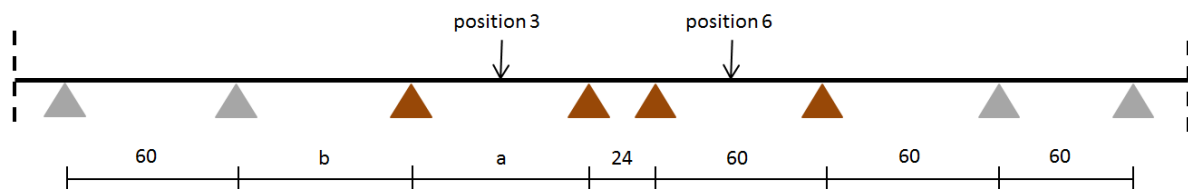


Figure 5.2: Sleeper distribution in the two sides of the joint (cm)

**Case 1:**  $a=50\text{cm}$ ,  $b=70\text{cm}$

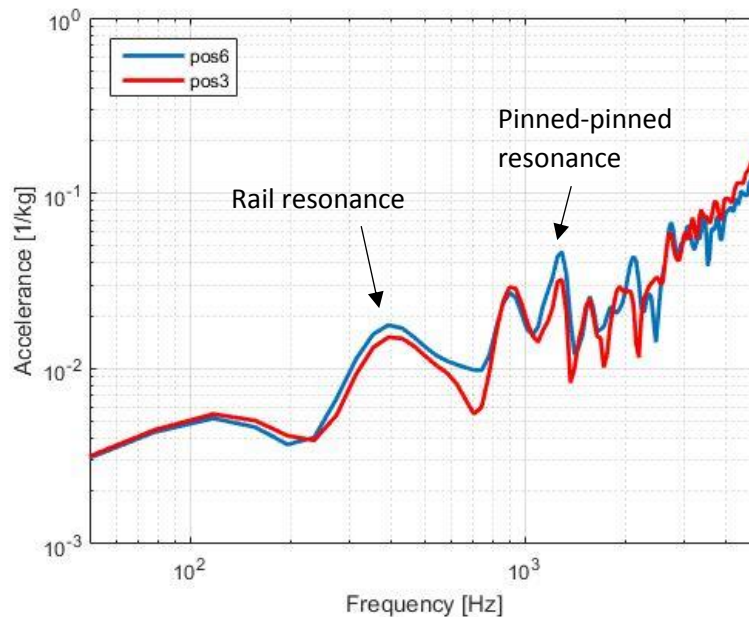


Figure 5.3: Comparison between uniform and non-uniform sleeper span. Case 1

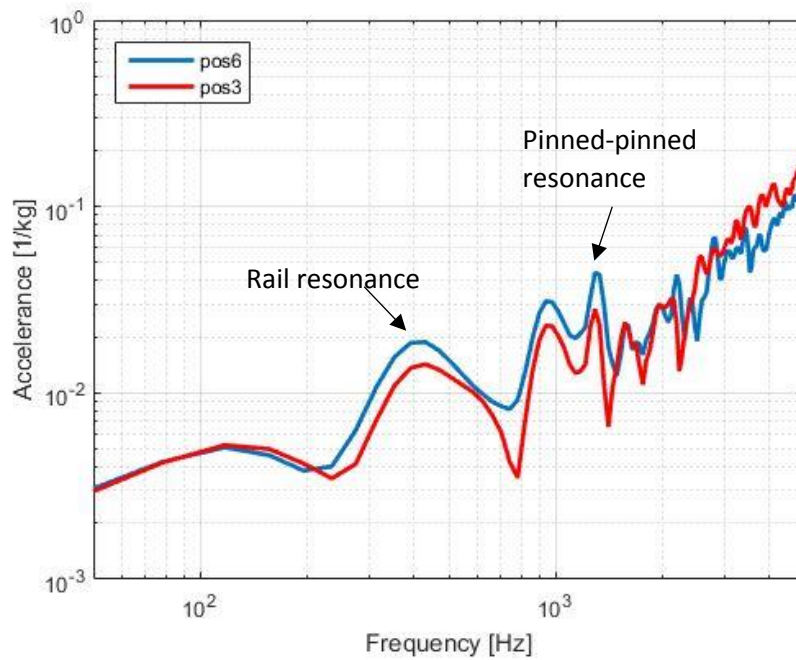
**Case 2:**  $a=40\text{cm}$ ,  $b=70\text{cm}$ 

Figure 5.4: Comparison between uniform and non-uniform sleeper span. Case 2

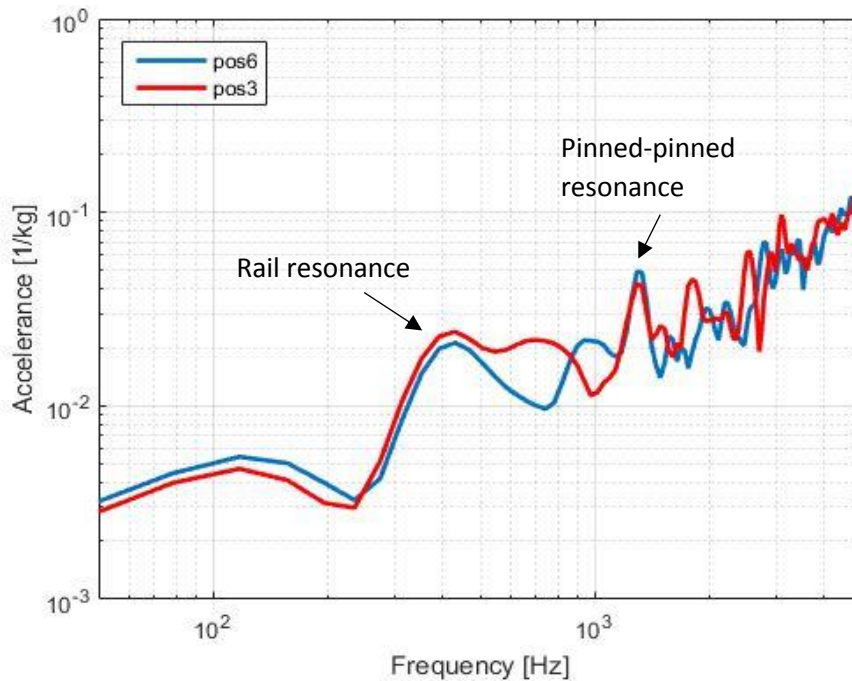
**Case 3:**  $a=70\text{cm}$ ,  $b=40\text{cm}$ 

Figure 5.5: Comparison between uniform and non-uniform sleeper span. Case 3

In the table below the reduction of the pinned-pinned resonance can be seen for all cases:

Case	Reduction (%)
1	30.5
2	36.2
3	13.2

Table 5.1: Percentage of reduction of pinned-pinned resonance for cases 1-3

### 5.3 Concluding remarks

Using the validated FE model, the findings obtained from the measurements, are confirmed. Applying a non-uniform distribution of the sleeper span, the pinned-pinned resonance can be reduced, because the wavelength of the standing wave does not fit anymore to the sleeper span. In particular, the more non-uniform the sleeper distribution is, the lower the amplitude for the pinned-pinned resonance is. It is also shown that for larger sleeper span, the rail resonance is higher. Finally, from figures 5.3-5.5 it is shown that the distance of the sleepers has a minimum or zero effect on the full track resonance. It is not possible to draw any conclusions for the high frequencies (more than 1400Hz) since the models are validated up to the frequency of 1400Hz.

# 6. Conclusions & recommendations

## 6.1 Conclusions

**The research questions proposed in section 1.1 can now be answered as follows:**

1. How do the NRG-joint and the normal joint respond to hammer excitation?

In the measurement results as well as in the two models applied, the characteristic vibration modes (full track resonance, rail resonance, sleeper anti-resonance and pinned-pinned resonance) were identified. The two joints have almost the same resonance frequencies, although their structure is different (different mass, length).

2. Does the NRG-joint behave better than the normal joint?

From the comparison between the FRFs of the two joints it seems at first glance that the NRG-joint behaves better than the normal joint, meaning that the amplitude of the vibrations is lower for the NRG-joint. However, a sound conclusion cannot be drawn, since the date at which the normal joint has been installed in the track is not known, so the differences in the behaviour of the two joints may also be attributed to their different operational conditions.

3. Which parameters affect the dynamic behaviour of the NRG-joint and the normal joint?

Ballast properties, rail-pad properties and sleeper spacing affect the dynamic behaviour of the system. Ballast properties affect the system behaviour in the middle frequency range (until 400Hz). Rail-pad properties influence the system behaviour in the middle and high frequency range (until 1100 Hz). They have a considerable effect on the frequency and the amplitude of the rail resonance and sleeper anti-resonance, while their effect is minimum regarding the pinned-pinned resonance. A more realistic representation of the rail-pads may affect the dynamic behaviour in a different way and in higher frequencies. Sleeper span and sleeper distribution play a dominant role in the amplitude and the frequency of the pinned-pinned resonance and affect also the other characteristic resonances (rail resonance, sleeper anti-resonance, but not the full track resonance).

4. How can the performance of the NRG-joint and the normal joint be optimised?

Combining field measurements observations and FRFs, a pattern was identified and later confirmed with the FE model: Employing a sleeper distribution with non-uniform sleeper distance leads to reduction of one of the significant track/rail resonances, the pinned-pinned resonance. More specifically, the more non-uniform the sleeper distribution is, the bigger the reduction of the pinned-pinned resonance.

## 6.2 Recommendations

Recommendations for further research can be summarized below:

- More hammer tests may be conducted to confirm the findings presented in this work.
- For the insulation layer laboratory tests are necessary in order to define properly its mechanical properties.
- Evaluation of the response and stress distribution of different insulation materials (e.g. fiberglass epoxy, Kevlar) against different types of loading (e.g. static, dynamic, cyclic).
- The numerical models for the NRG and the normal joint can be both used for other type of analysis such as wheel-rail contact interaction. Using explicit FEM, wheel-rail rolling from single-point to two-point contact can be investigated for the two joints, in order to estimate their differences in the response. Pass-by measurements may be conducted to validate the results.
- More realistic representation of the rail-pads using solid elements, may result in better fit between the model and the measurements.
- More sleeper distributions may be examined in order to identify the optimum case, that reduces the pinned-pinned resonance.
- Standardization of the hammer test as an instrument for the evaluation of the dynamic behaviour and detection of damages that cannot be seen by naked eye.
- Comparison between the NRG and the normal joint, preferably with laboratory measurements, or with more field measurements (where the operational conditions of both joints will be known), in order to draw a concrete conclusion.
- Fatigue tests combined with FEM modelling in order to evaluate the behaviour of the NRG-joint against cyclic loading.
- Optimization of the NRG-joint in terms of materials and geometry.
- More realistic representation of the bolts using their nominal geometry.

# Appendices

## Appendix A: ANSYS elements

### SOLID185 Element Description [54]

SOLID185 is used for 3-D modelling of solid structures. It is defined by eight nodes having three degrees of freedom at each node: translations in the nodal x, y, and z directions. The element has plasticity, hyperelasticity, stress stiffening, creep, large deflection, and large strain capabilities. It also has mixed formulation capability for simulating deformations of nearly incompressible elastoplastic materials, and fully incompressible hyperelastic materials.

SOLID185 is available in two forms:

- Homogeneous Structural Solid (KEYOPT(3) = 0, the default)
- Layered Structural Solid (KEYOPT(3) = 1)

A higher-order version of the SOLID185 element is [SOLID186](#).

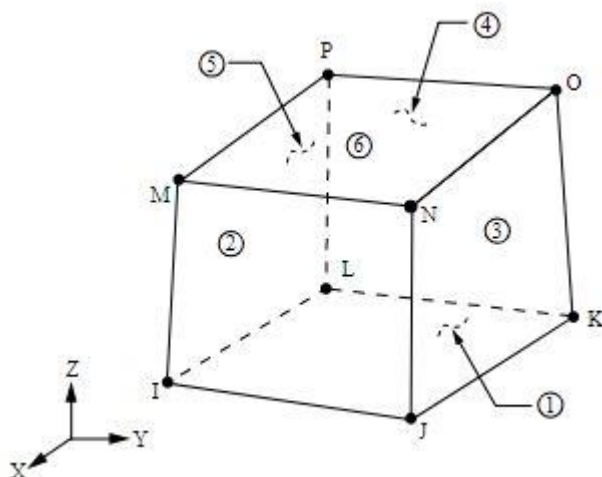


Figure A.0.1: Solid185 Structural Solid Geometry [54]

### SOLID164 Element Description

SOLID164 is used for the 3-D modeling of solid structures. The element is defined by eight nodes having the following degrees of freedom at each node: translations, velocities, and accelerations in the nodal x, y, and z directions.

## COMBIN14 Element Description [55]

COMBIN14 has longitudinal or torsional capability in 1-D, 2-D, or 3-D applications. The longitudinal spring-damper option is a uniaxial tension-compression element with up to three degrees of freedom at each node: translations in the nodal x, y, and z directions. No bending or torsion is considered. The torsional spring-damper option is a purely rotational element with three degrees of freedom at each node: rotations about the nodal x, y, and z axes. No bending or axial loads are considered.

The spring-damper element has no mass. Masses can be added by using the appropriate mass element ([MASS21](#)). The spring or the damping capability may be removed from the element. A general spring or damper is also available in the stiffness matrix element ([MATRIX27](#)). Another spring-damper element (having its direction of action determined by the nodal coordinate directions) is [COMBIN40](#).

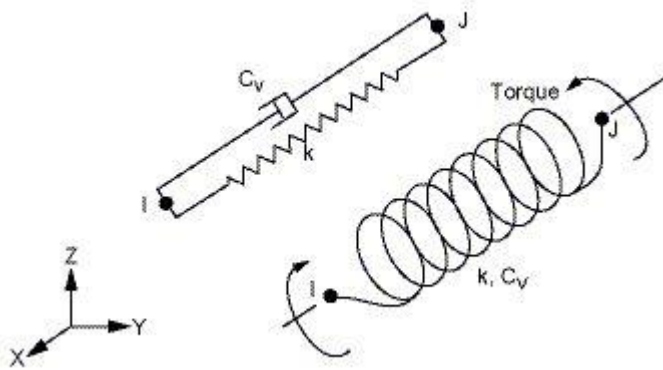


Figure A.0.2: COMBIN14 Geometry [55]

## COMBI165 Element Description

COMBI165 allows you to model simple spring or damper systems, as well as the response of more complicated mechanisms such as the energy absorbers used in passenger vehicle bumpers. These mechanisms are often experimentally characterized in terms of force-displacement curves. This element provides a variety of discrete element formulations that can be used individually or in combination to model complex force-displacement relations.

COMBI165 is a two-node, 1-D element. You cannot define both spring and damper properties for the same element. Separate spring and damper elements are required, but they may use the same nodes (that is, you can overlay two different COMBI165 elements). A COMBI165 element can be attached to any of the other explicit elements.

## CONTA174 Element Description

CONTA174 is used to represent contact and sliding between 3-D target surfaces and a deformable surface defined by this element. The element is applicable to 3-D structural and coupled-field contact analyses. It can be used for both pair-based contact and general contact.

In the case of pair-based contact, the target surface is defined by the 3-D target element type, [TARGE170](#). In the case of general contact, the target surface can be defined by CONTA174 elements (for deformable surfaces) or [TARGE170](#) elements (for rigid bodies only). Contact occurs when the element surface penetrates an associated target surface. Coulomb friction, shear stress friction, user-defined friction with the USERFRIC subroutine, and user-defined contact interaction with the USERINTER subroutine are allowed. The element also allows separation of bonded contact to simulate interface delamination.

## TARGE170 Element Description

TARGE170 is used to represent various 3-D "target" surfaces for the associated contact elements ([CONTA173](#), [CONTA174](#), [CONTA175](#), [CONTA176](#), and [CONTA177](#)). The contact elements themselves overlay the solid, shell, or line elements describing the boundary of a deformable body and are potentially in contact with the target surface, defined by TARGE170. You can impose any translational or rotational displacement, temperature, voltage, and magnetic potential on the target segment element. You can also impose forces and moments on target elements. See [TARGE170](#) in the *Mechanical APDL Theory Reference* for more details about this element. To represent 2-D target surfaces, use [TARGE169](#), a 2-D target segment element. For rigid target surfaces, these elements can easily model complex target shapes. For flexible targets, these elements will overlay the solid, shell, or line elements describing the boundary of the deformable target body.

## Appendix B: Augmented Lagrange Method [56]

For nonlinear solid body contact of faces, **Pure Penalty** or **Augmented Lagrange** formulations can be used. Both of these are penalty-based contact formulations:

$$F_{\text{Normal}} = k_{\text{Normal}} x_{\text{Penetration}}$$

The finite contact Force,  $F_n$ , is a concept of contact stiffness,  $k_{\text{Normal}}$ . The higher the contact stiffness, the lower the penetration,  $x_p$ , as illustrated here.

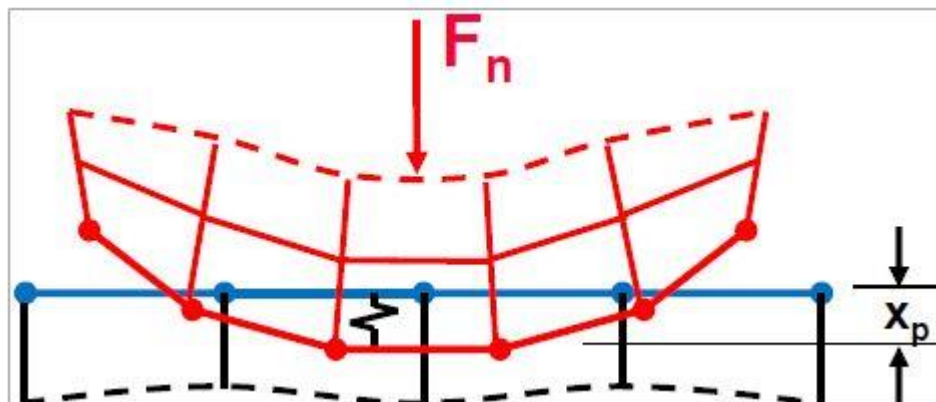


Figure A.3: Contact formulation [56]

Ideally, for an infinite  $k_{\text{Normal}}$ , one would get zero penetration. This is not numerically possible with penalty-based methods, but as long as  $x_p$  is small or negligible, the solution results are accurate.

The main difference between Pure Penalty and Augmented Lagrange methods is that Augmented Lagrange augments the contact force (pressure) calculations:

Pure Penalty:  $\mathbf{F}_{\text{Normal}} = \mathbf{k}_{\text{Normal}}\mathbf{x}_{\text{Penetration}}$

Augmented Lagrange:  $\mathbf{F}_{\text{Normal}} = \mathbf{k}_{\text{Normal}}\mathbf{x}_{\text{Penetration}} + \lambda$

Because of the extra term  $\lambda$ , the Augmented Lagrange method is less sensitive to the magnitude of the contact stiffness  $k_{\text{Normal}}$ .

## References

1. Various. *Rail transport*. Available from: [https://en.wikipedia.org/wiki/Rail\\_transport](https://en.wikipedia.org/wiki/Rail_transport).
2. ProRail. *Rail transport in the Netherlands*. Available from: [https://en.wikipedia.org/wiki/Rail\\_transport\\_in\\_the\\_Netherlands](https://en.wikipedia.org/wiki/Rail_transport_in_the_Netherlands).
3. Oregui Echeverria-Berreyarza, M., *Vertical railway track dynamics: from measurements to numerical modelling*. 2015, TU Delft, Delft University of Technology.
4. Robinson, D.W., G.R.S. Company, Editor. 1872: United States.
5. 2013; Available from: <http://www.railsystem.net/track-circuit/>.
6. Gallou, M., et al., *Potential for external reinforcement of insulated rail joints*. Proceedings of the Institution of Mechanical Engineers, Part F: Journal of Rail and Rapid Transit, 2018. **232**(3): p. 697-708.
7. Peltier, D.C., *Measuring and Evaluating Progressive Epoxy Debonding in Bonded Insulated Rail Joints*. 2008, University of Illinois at Urbana-Champaign.
8. Davis, D.D., et al. *Effects of heavy axle loads on bonded insulated joint performance*. in *Proceedings of the AREMA 2005 Annual Conference*. 2005.
9. Transportation, U.S.D.o., *Update of Heavy Axle Load Revenue Service Testing at Mega Sites in Revenue Service*. 2008.
10. Report, R.S.I., *Derailment of Pacific National's Ore Service*. 2006.
11. Report, R.A., *Derailment of Canadian Pacific Railway Freight Train 292-16 and subsequent release of Anhydrous Ammonia near Minot*. 2002.
12. Report, R.A., *Derailment of Union Pacific Railroad Train QFPLI-26 at Eunice, Louisiana*. 2000.
13. ProRail, A.A.e.T., *Best Practice inspectie en onderhoud van ES-lassen*. 2014.
14. Zong, N., *Development of optimal designs of insulated rail joints*. 2013, Queensland University of Technology.
15. Papatsakona, K. *Νεκροί και πολλοί τραυματίες από εκτροχιασμό τρένου στην Ιταλία*. 2018; Available from: <http://www.zougla.gr/kosmos/article/italia-ektroxiasmos-amaksostixias-konta-sto-milano---dio-nekri>.
16. Barbero, E.J., *Introduction to composite materials design*. 2017: CRC press.
17. Kerr, A.D. and J.E. Cox, *Analysis and tests of boned insulated rail joints subjected to vertical wheel loads*. International Journal of Mechanical Sciences, 1999. **41**(10): p. 1253-1272.
18. Suzuki, T., et al., *Measurement on dynamic behaviour of track near rail joints and prediction of track settlement*. Quarterly Report of RTRI, 2005. **46**(2): p. 124-129.
19. Kitagawa, T., et al., *Experimental and theoretical studies on impact noise generation due to rail joints*, in *Noise and Vibration Mitigation for Rail Transportation Systems*. 2015, Springer. p. 55-62.
20. Talamini, B., D.Y. Jeong, and J. Gordon. *Estimation of the fatigue life of railroad joint bars*. in *ASME/IEEE 2007 Joint Rail Conference and Internal Combustion Engine Division Spring Technical Conference*. 2007. American Society of Mechanical Engineers.
21. Himebaugh, A.K., R.H. Plaut, and D.A. Dillard, *Finite element analysis of bonded insulated rail joints*. International Journal of Adhesion and Adhesives, 2008. **28**(3): p. 142-150.
22. Mandal, N.K. and M. Dhanasekar, *Sub-modelling for the ratchetting failure of insulated rail joints*. International Journal of Mechanical Sciences, 2013. **75**: p. 110-122.
23. Ding, K. and M. Dhanasekar, *Flexural behaviour of bonded-bolted butt joints due to bolt looseness*. Advances in Engineering Software, 2007. **38**(8-9): p. 598-606.
24. Sandström, J. and A. Ekberg, *Numerical study of the mechanical deterioration of insulated rail joints*. Proceedings of the Institution of Mechanical Engineers, Part F: Journal of Rail and Rapid Transit, 2009. **223**(3): p. 265-273.

25. Bandula-Heva, T. and M. Dhanasekar, *Failure of discontinuous railhead edges due to plastic strain accumulation*. Engineering Failure Analysis, 2014. **44**: p. 110-124.
26. Mandal, N.K. and B. Peach, *An engineering analysis of insulated rail joints: a general perspective*. Int J Eng Sci Technol, 2010. **2**(8): p. 3964-88.
27. Man, A.P.d., *DYNATRACK: A survey of dynamic railway track properties and their quality*. 2002.
28. Yang, Z., et al., *Numerical and experimental study of wheel-rail impact vibration and noise generated at an insulated rail joint*. International Journal of Impact Engineering, 2018. **113**: p. 29-39.
29. Esveld, C. and A. De Man. *Use of railway track vibration behaviour for design and maintenance*. in *IABSE Symposium Report*. 2003. International Association for Bridge and Structural Engineering.
30. Kaewunruen, S. and A. Remennikov, *Non-destructive testing (NDT): a tool for dynamic health monitoring of railway track structures*. 2006.
31. Oregui, M., et al., *Experimental investigation into the condition of insulated rail joints by impact excitation*. Experimental Mechanics, 2015. **55**(9): p. 1597-1612.
32. Oregui, M., et al. *A 3D finite element modeling of hammer test for track parameter identification*. in *ICEDyn 2011: Proceedings of the International Conference on Structural Engineering Dynamics, Tavira, Portugal, 20-22 June 2011*. 2011. Citeseer.
33. Sadri, M. and M. Steenbergen, *Effects of railway track design on the expected degradation: Parametric study on energy dissipation*. Journal of Sound and Vibration, 2018. **419**: p. 281-301.
34. Zakeri, J.A. and H. Xia, *Sensitivity analysis of track parameters on train-track dynamic interaction*. Journal of Mechanical Science and Technology, 2008. **22**(7): p. 1299-1304.
35. Akhtar, M., D. Davis, and T. O'Connor, *Revenue service evaluation of advanced design insulated joints*. Transportation Technology Center, Inc. Pueblo, CO, 2008.
36. Inc., K.; Available from: <https://www.progressiverailroading.com/railproducts/product.aspx?id=4873>.
37. IMTRAM. Available from: <http://imtram.com/imtram-products/rail-joints/comply-insulated-rail-joints/>.
38. Plaut, R.H., et al., *Analysis of tapered, adhesively bonded, insulated rail joints*. Proceedings of the Institution of Mechanical Engineers, Part F: Journal of Rail and Rapid Transit, 2007. **221**(2): p. 195-204.
39. Charlton, Z., *Innovative design concepts for insulated joints*. 2007, Virginia Tech.
40. Rewczuk, C. *Insulated Joint Studies*. Available from: [https://www.arena.org/files/library/2013\\_Conference\\_Proceedings/Insulated\\_Joint\\_Studies.pdf](https://www.arena.org/files/library/2013_Conference_Proceedings/Insulated_Joint_Studies.pdf).
41. Technology, S.M., *UNIE200 Technical Data Sheet*. 2008.
42. Wikipedia. Available from: [https://en.wikipedia.org/wiki/Meppel%E2%80%93Groningen\\_railway](https://en.wikipedia.org/wiki/Meppel%E2%80%93Groningen_railway).
43. *Marsweg*. 2018.
44. Goodman, J.R. and J. Bodig, *Orthotropic elastic properties of wood*. Journal of the Structural Division, 1970. **96**(11): p. 2301-2319.
45. Mackenzie-Helnwein, P., et al., *Analysis of layered wooden shells using an orthotropic elasto-plastic model for multi-axial loading of clear spruce wood*. Computer methods in applied mechanics and engineering, 2005. **194**(21-24): p. 2661-2685.
46. Tabiei, A. and J. Wu, *Three-dimensional nonlinear orthotropic finite element material model for wood*. Composite structures, 2000. **50**(2): p. 143-149.
47. Nielsen, J.C., E. Kabo, and A. Ekberg, *Alarm limits for wheel-rail impact loads—part 1: rail bending moments generated by wheel flats*. 2009, Chalmers University of Technology.

48. Sudheer, M., K. Pradyoth, and S. Somayaji, *Analytical and Numerical validation of epoxy/glass structural composites for elastic models*. American Journal of Materials Science, 2015. **5**(3C): p. 162-168.
49. Tita, V., J.d. Carvalho, and J. Lirani, *Theoretical and experimental dynamic analysis of fiber reinforced composite beams*. Journal of the Brazilian Society of Mechanical Sciences and Engineering, 2003. **25**(3): p. 306-310.
50. Younes, R., et al., *Comparative review study on elastic properties modeling for unidirectional composite materials*, in *Composites and their properties*. 2012, intech.
51. University, M.T.; Available from: <http://www.mse.mtu.edu/~drjohn/my4150/props.html>.
52. MatWeb. Available from:  
<http://www.matweb.com/search/datasheet.aspx?matguid=3f2253a553404b13893830617250b5d8&ckck=1>.
53. De Man, A., *Pin-pin resonance as a reference in determining ballasted railway track vibration behaviour*. HERON-ENGLISH EDITION-, 2000. **45**(1): p. 35-52.
54. *SOLID185 Element Description*. 2015; Available from:  
[https://www.sharcnet.ca/Software/Ansys/16.2.3/en-us/help/ans\\_elem/Hlp E SOLID185.html](https://www.sharcnet.ca/Software/Ansys/16.2.3/en-us/help/ans_elem/Hlp E SOLID185.html).
55. *COMBIN14 Element Description*. 2016; Available from:  
[https://www.sharcnet.ca/Software/Fluent14/help/ans\\_elem/Hlp E COMBIN14.html](https://www.sharcnet.ca/Software/Fluent14/help/ans_elem/Hlp E COMBIN14.html).
56. *Contact Formulation Theory*. 2016; Available from:  
[https://www.sharcnet.ca/Software/Ansys/17.0/en-us/help/wb\\_sim/ds\\_contact\\_theory.html](https://www.sharcnet.ca/Software/Ansys/17.0/en-us/help/wb_sim/ds_contact_theory.html).